POLITECNICO DI TORINO

Master's Degree in Mechatronics Engineering
Software Technologies for Automation

MODELING, CONTROL AND CHARACTERIZATION OF AN ELECTRODYNAMIC LEVITATION TEST BENCH

Supervisors:
Prof. Andrea TONOLI
Prof. Nicola AMATI
Prof. Angelo BONFITTO
Dr. Renato GALLUZZI
Dr. Salvatore CIRCOSTA

Candidate:
Andrea BO

Graduation's session July 2022
Academic Year 2021/2022

ABSTRACT

In recent years, it is becoming increasingly evident the need to counteract gas emissions in order to drastically reduce the impact of the human species on the planet and the need to find new sustainable solutions in every aspect of everyday life. In the field of mobility and transport, the Hyperloop concept, a high-speed transport system for passengers and goods based on the magnetic levitation principle, could potentially represent a radical breakthrough for the mobility of the future. The central and key factor of the whole project lies in the stability of the electrodynamic levitation system. Some recent studies in literature have proposed to replicate the electrodynamic behaviour through the use of a lumped-parameter model consisting of a multiple-branch circuit. Through such an approach it is feasible to model the interaction between the mechanical and the electrical domains, in the context of LTI systems, and it became possible to identify the unstable nature of the system. The objective of the thesis is the assembly, set up and characterization of a test bench for conducting experimental tests on a Hyperloop-like levitation device. At first, the conduction of experimental tests of quasi-static nature and the measurement of the forces involved during operation allow the tuning and validation of the novel lumped parameter model. The identification of the unstable nature of the system and the quantification of the margin of instability that is necessary to fill through the use of a secondary suspension leads to the multibody modeling of the system, the simulation of different control strategies and the comparison of the performance of the different techniques. Finally, the foundations are laid for a sensor less estimation of the velocities of the different masses involved in the dynamics of the system.

Acknowledgements

Foremost, i would like to express my special thanks of gratitude to Professor Andrea Tonoli and Professor Nicola Amati who gave me the opportunity to participate in this exciting, challenging and ambitious project . My sincere thanks also goes to Professor Angelo Bonfitto, Dr. Salvatore Circosta and Luis Castellanos for the valuable advice and support. A special thanks goes to Eugenio Tramacere and Dr. Renato Galluzzi, with patience and dedication they guided my work during all the months of my thesis and, through their passion for engineering they supported, motivated and encouraged me to work hard. I would also like to thank my colleague Arianna Conchin Gubernati, with whom I shared the journey and the last months of my experience in the master's degree course.

To my parents, I thank you from the bottom of my heart for supporting me in difficult times, for sharing with me moments of joy, for loving me always and for allowing me to pursue my goals. To my friends, who have been close to me during all the years of university and who have been able to understand moments of difficulty and have always had a right word at the right time.

Sincerely, thank you.

Andrea

Table of Contents

List of Figures

List of Tables

Chapter 1

Introduction

The objective of the present dissertation is to conduct experiments of quasi-static and dynamic nature on a magnetic levitation system based on the Hyperloop concept, the validation of a lumped parameter RL model for the modeling of the electrodynamic levitation phenomenon and the stability control of the system through the implementation of a secondary suspension.
It is developed at the *Machatronics Lab* (LIM) based in the *Politecnico di Torino* and in collaboration with the US company *Hyperloop Transportation Technologies*.
In this chapter the Hyperloop system will be introduced with its main characteristics and the advantages and disadvantages that it implies. Finally, after a brief explanation of the literature and the state of the art, the objectives and organization of the discussion will be outlined precisely.

1.1 The Hyperloop paradigm

Hyperloop, defined by some as "The Fifth Mode of Transportation" [1], is a high-speed transport system for passengers and goods based on the magnetic levitation principle that in the last decade has received increasing attention and is considered by many a radical breakthrough for the mobility of the future. It is a fast and reliable method of transport that can be used as an alternative to air travel for long or medium distances, allowing them to be covered in a minimum amount of time. The prospects of Hyperloop are not only linked to an innovative and technological factor such as improvements in travel time and comfort, but also to the urgency of finding reliable solutions to the climate crisis we are facing. In recent years it is becoming increasingly evident the need to counteract the use of fossil fuels and greenhouse gas emissions in order to drastically reduce the impact of the human species on the planet. As stated by Virgin Hyperloop CEO Josh Giegel, a system based on the magnetic levitation principle as Hyperloop fits perfectly into this framework, allowing to drastically reduce air pollution and fitting optimally as a missing link between the rail market and the aeronautical market [2].

1.1.1 Hystorical background

The origin of the concept dates back to the early decades of the twentieth century when Robert Goddard, a university student in those years, hypothesized a new typology of transport similar to the railway but based on Maglev technology for levitation and propulsion and the use of an infrastructure made by tubes subjected to high vacuum [3]. The train in question would have the capacity to reach 1600 km / h, making it possible to make the journey from Boston to New York in just 12 minutes. However, the student's projects were made public only after his death in 1945.

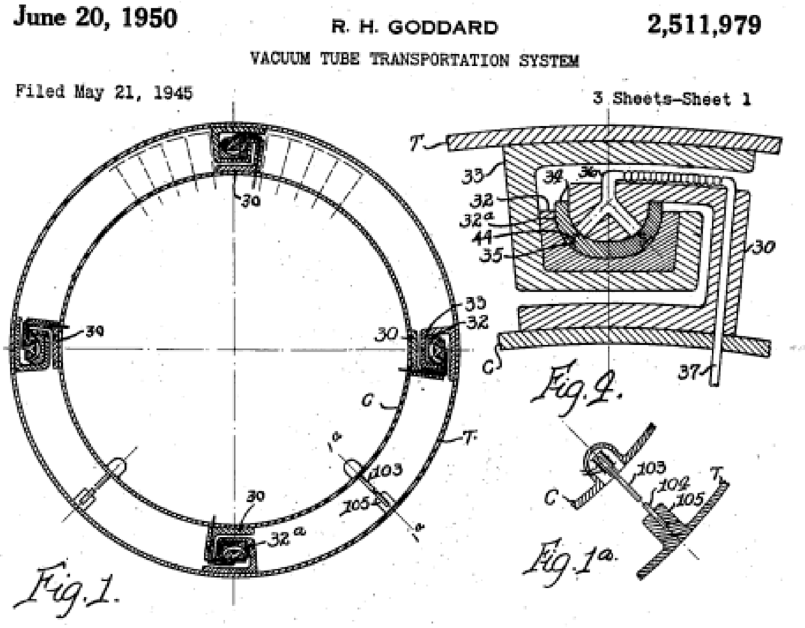

Figure 1.1: Qualitative sketches by Robert Goddard [3].

The railway transport based on the magnetic levitation principle is applied in the Maglev technology, introduced by a patent dating back to 1934 by the German engineer Hermann Kemper. The development of this technology has crossed the twentieth century reaching its implementation in 2003 in Shanghai. The operating principle of a Maglev train is based on the use of attractive or repulsive magnetic fields between the electromagnets (or permanent magnets) that generate them and a guide. Propulsion, instead, is achieved through the use of a linear electric motor. The absence of contact between the wheels and the rails employed in the normal railway transport system implies a drastic reduction of friction forces, which are represented only by air resistance and for this reason Maglev trains can reach speeds up to 600 Km/h. Moreover, this also implies a lower maintenance cost resulting from the wear and tear of wheels and rails previously used. But this is not the only advantage implied by the use of this technology. The absence of wheels eliminates annoying vibrations and noise, the absence of contact prevents slipping and sliding, and greater acceleration and deceleration can be achieved [4].

Figure 1.2: Maglev Transrapid, Shangai[1].

Although the advantages introduced by this technology are many, Maglev trains are scarcely used nowadays. In fact, the cost of a Maglev train ticket is on average higher than the cost of an airplane ticket and the speeds that can be reached do not allow to decrease the travel time.

In this scenario, the modern concept of Hyperloop was born. In 2013 Elon Musk, South African engineer and tycoon, publishes a white paper entitled *Hyperloop Alpha*. Compared to Maglev technology, whose speed is limited by the force of air resistance, a new type of infrastructure is studied, composed of tubes inside which is maintained a controlled environment of low air pressure in which capsules containing passengers can travel. A further difference with Maglev technology lies in the technology exploited to obtain the lifting effect and transport of the capsules. While in the first case the magnetic levitation principle was considered, in the case of Hyperloop Alpha an air bearing system would be used to obtain the same effect. In addition, each of the capsules would be equipped with an electric compressor fan installed in the front of the vehicle with the aim of transferring high-pressure air from the front to the rear of the latter. As far as propulsion

---

1 ethicforge.cc, 20th March 2019, Should Maglev trains be further developed?, URL: https://www.ethicsforge.cc/should-maglev-trains-be-further-developed/

is concerned, linear electric motors would be used to accelerate the capsules to a speed higher than 1220 Km/h [5]. Some qualitative sketches present within the original paper are depicted in figure 1.3.

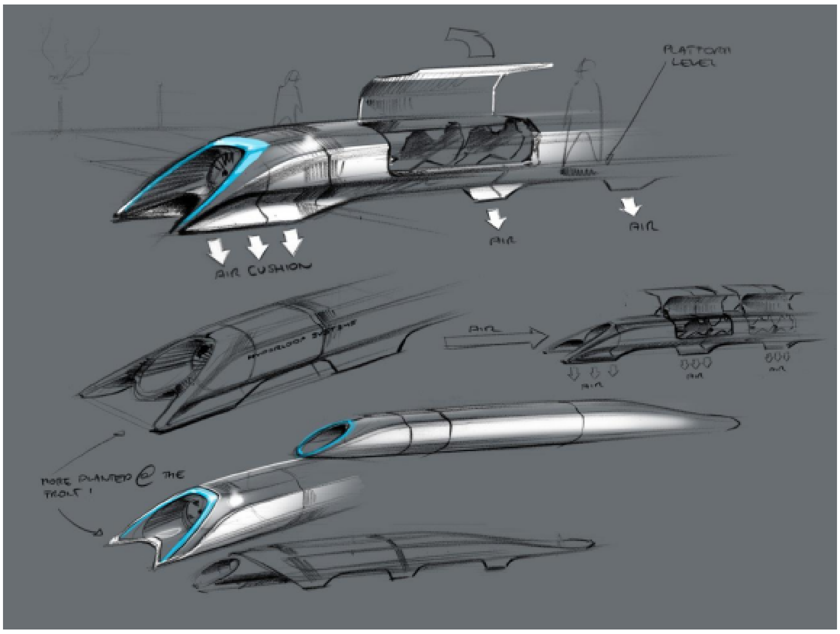

Figure 1.3: Hyperloop Alpha qualitative sketches [5].

The project outlined within this paper was never actually realized, but the current Hyperloop concept that companies like *Hyperloop Transportation Technologies* are actively working on shares several aspects with Elon Musk's 2013 project. The working principle of Hyperloop will be briefly described in the next subsection.

1.1.2 Operating principle

The Hyperloop operating principle is based on the Inductrack concept [6] introduced by Richard F. Post and Dimitri Ryutov in 1996. The air bearing system used to obtain a levitation effect in the Hyperloop Alpha project is replaced by magnetic pads that, thanks to the interaction with static tracks of electrically conductive material, produce magnetic levitation and guidance. The magnetic pads consist of special configurations of permanent magnets that introduce peculiar properties into the system. A Halbach Array consists in a precise arrangement of the magnetic moment vectors of each permanent magnet that is part of the configuration. It is represented in the figure 1.4

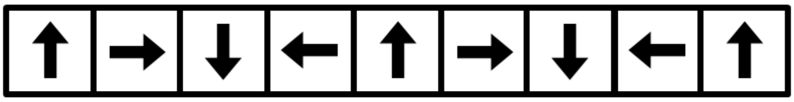

Figure 1.4: Halbach Array configuration.

Introducing an array arrangement of this type can be advantageous since the resulting magnetic field on one side of the configuration (in the case of figure 1.4 the inferior side) is greatly strengthened, while on the opposite side (superior side) it is almost totally cancelled by interference. This type of configuration can be crucial both with respect to the magnetic levitation principle and with respect to the point of view of shielding passengers from the remarkably strong magnetic fields generated by the permanent magnets at the bottom of the pods.
The relative motion of the permanent magnets of the pad with respect to the electrically conducting tracks induce eddy currents which in turn generate a magnetic field that opposes the field that generated it by the Faraday-Neumann-Lenz law. The result is that two force components are exerted on the pod, perpendicular to each other: a levitation force F_{lift} and a friction force in the opposite direction to the pod's direction of motion F_{drag}. The lift to drag ratio increases as the speed increases, which makes the system particularly attractive for applications working at high speeds. A non-negligible disadvantage of this system is that magnetic levitation based on permanent magnets has an inherently unstable behavior.
The infrastructure within which the pods travel is similar to that illustrated in the Hyperloop Alpha white paper, i.e. tubes in which a controlled low-pressure environment is maintained to minimize the friction forces arising from air resistance. The pods are propelled by a linear electric induction motor.

1.2 Literature review and state of the art

In this section a review of the literature published so far on the topic and the current state of the art will be conducted in order to contextualize the present discussion and clarify the starting points on which it is based.

In the last decade there has been an increasing interest in future transportation systems based on sustainable, safe, reliable and fast technologies of which the

Hyperloop concept is a part. However, although these aspects are currently addressed by several government programs that fund research and development in this area, some fields such as passive electrodynamic levitation remain partially unexplored. The main goal of current research is to identify and analytically model the intrisic instability of passive electrodynamic levitation-based systems and to develop stabilization techniques, taking into account the electrodynamic phenomena, the mechanical domain, and the strong correlation and interaction between them.

In this context, a solid foundation is represented by the research carried out over the years by research groups such as Tonoli et al. ([7], [8], [9], [10]), Filatov and Maslen [11] and Lembke ([12], [13] [14], [15]) on modeling and identifying the unstable nature of electrodynamic bearings (EDBs) and implementing different stabilization techniques and, similarly, Van Verdeghem et al. ([16], [17]) with their research in the field of rotational systems equipped with thrust EDBs. The phenomenon of passive electrodynamic levitation of moving pods can be considered as the translational counterpart that shares the behavior and unstable nature with the corresponding rotational dynamics, and therefore need stabilization. In this regard, research conducted by Post et al. ([6], [18], [19]) in the context of the Inductrack project led to the modeling of the phenomenon, although in the subsequent experimental campaign the unstable nature was not observed.

Storset et al. [20], in 2002, demonstrated that a passive electrodynamic levitation system inherently exhibits low damping behavior and therefore the application of stabilization techniques is required to ensure a stable and safe behavior.

In the same year, General Atomics built a full-scale working prototype for testing the levitation and propulsion system located at General Atomics Electromagnetics Systems in San Diego, California. The test track is 120m long and includes a 50m radius curve for vehicle guidance testing ([21], [22]). During the experimental phases it was observed that in several cases a larger than expected air gap was reached and, since the vertical movement was limited by the contact of the auxiliary wheels, this could affect the dynamics of the system and mask the unstable nature. General Atomics also built a test bench to reproduce the forces behavior during the passive electrodynamic levitation phenomenon. The result of the experiments shows that at high speeds, strongly nonlinear contributions are introduced and thus the difficulty in analytically modeling the behavior of the forces ([23], [24]).

From 2015 to 2019, teams of students had the opportunity to participate in the SpaceX Hyperloop Pod Competition, an annual competition funded by SpaceX with the goal of designing a small-scale pod prototype with the intention of demonstrating the technical feasibility of some aspect of Hyperloop ([25], [26]).

Recently, research conducted by Guo et al. [27] has shown that it is possible to analytically study the system using an electrical circuit based model with the objective of deriving the static levitation forces from the governing electrodynamic laws. The approach followed is nonlinear and is based on the magnetic vector potential approach. However, the research does not consider the dynamics of the mechanical domain and the coupling between it and the electromagnetic domain, and for this reason it is not possible to model the instability phenomena.

1.2.1 Multi-domain approach to the stabilization of electrodynamic levitation systems and passive multi-dof stabilization

The researches and studies on which the present discussion is mainly based concern a multi-domain approach (electrodynamic domain and mechanical domain) to the stabilization of an electrodynamic levitation system conducted by Galluzzi et al. [28] and the study of a passive stabilization applied to multiple degrees of freedom of ultra-high-speed maglev vehicles by Circosta et al. [29].
The work of Galluzzi et al. is aimed at determining a model for reproducing the intrisic stability of electrodynamic levitation systems. It uses a multiple branch RL electrical circuit for modeling the electromechanical domain. In this framework, it is necessary to implement model parameter identification techniques and for this reason data collected from finite element simulations (FEM) are fitted to the linear time invariant (LTI) model with the aim of optimizing the number of branches of the circuit in terms of accuracy and model complexity. Instability in levitation systems arises from the interaction between the electrodynamic domain and the mechanical domain but it takes place only in the mechanical degrees of freedom. The only possibility to analytically model such an instability is to consider a multi-domain approach and then establish a methodology for stabilizing the system using tools such as the root locus method and with the introduction of a properly controlled secondary suspension.
The work of Circosta et al., on the other hand, aims to extend the methodology used by Galluzzi et al. for vertical dynamics to all degrees of freedom of the system in order to implement full electrodynamic levitation.

1.3 Thesis goal and outline

The objective of the thesis is the validation of a multi-domain modelling technique proposed by Galluzzi et al. through experimentation on a test bench that simulates the phenomenon of passive electrodynamic levitation of Hyperloop on a laboratory scale. The test bench, designed by Fanigliulo [30], must be made operational with the appropriate instrumentation for signal acquisition and general system operation. In addition, it was deemed necessary to accurately model the system using tools such as *Matlab* & *Simulink* (in particular *Simulink Simscape Multibody*) which allow the simulation of its behaviour and the simulation of different control techniques with regard to dynamic stabilisation. The need to implement control techniques with the aim of stabilising the system implies the detection and acquisition of a whole series of signals describing the precise behaviour of the dynamic system. For this reason, sensorless signal detection techniques have been evaluated and simulated with regard to the secondary suspension used to ensure the stability of the system.

The remainder of the discussion is organized as follows.
Chapter 2 opens with a description of the test bench and its components and of the quasi-static and dynamic measurement stages. Following, the description of different characterization procedures on different elements of the test bench and the presentation of the type of permanent magnets array treated in the thesis.
Chapter 3 deals with everything related to quasi-static analysis and experimental tests conducted on the test bench. The chapter presents the experimental results and deals with the tuning of the lumped parameters for the analytical modelling of the interaction between mechanical and electrical domain and the identification of system instability.
Chapter 4 presents different control strategies and compares the performance of each of them through simulation and the use of a multibody model of the system developed in *Matlab* & *Simulink*.
Finally, the fifth and final chapter introduces two different speed estimation techniques with the aim of verifying through simulation the feasibility of a sensorless estimation, fundamental for the implementation of the control strategies discussed in the previous chapter.

Chapter 2

Test bench

The following chapter provides a general description of the test bench and its main components, together with the characterisation of some of them such as the copper track and the aluminium disc. In addition, the layouts of the measurement stages used for the quasi-static analysis and the dynamic analysis of the system are presented. In this context, some of the constituent elements of the measuring stages, such as load cells for the quasi-static measuring stage and springs for the dynamic measuring stage, need to be described and characterised in more detail.

2.1 General description

The structure of the test bench consists of a main frame made of different materials depending on the different functions of its parts. At the bottom, the frame is made of AISI 1035 (SS) steel and forms the four supports of the test bench. The upper part of the main frame consists of two plates made of aluminium alloy to avoid interference during the mounting and positioning of the magnetic structures (Halbach arrays) which are part of the measurement stages described in the following sections, and four plates made of rigid and transparent PVC which allow visual monitoring of the system and ensure safety during the conduction of the experimental tests.
The copper track is supported by an aluminium disc rigidly connected to a central shaft. The latter is connected to an electric motor via a torsional joint and is held in position by single row angular contact ball bearings that allow it to rotate. An omega-shaped structure made of plastic material protects the joint and the rotating elements during operation and allows the attachment of the electric motor, which is thus kept in a raised position with respect to the ground. A sectional representation of the test bench is shown in figure 2.1.

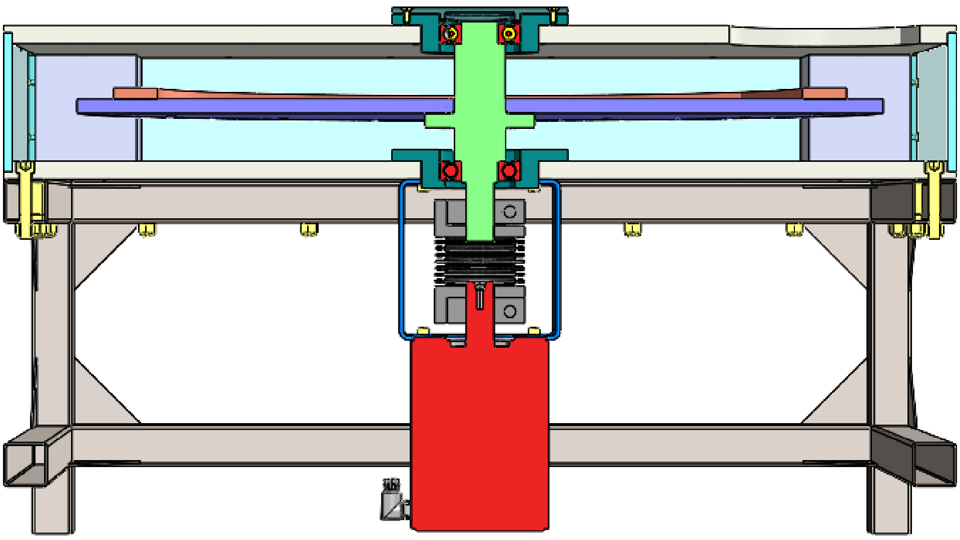

Figure 2.1: Sectional view of the test bench. Courtesy of Dr. A. Bonfitto, Eng. E.C. Zenerino and A. D'Oronzo.

The electric motor implemented is a Kollmorgen AKM74L (datasheet in [31]), while a Kollmorgen AKD inverter is used to control it (datasheet in [32]).

The table below shows the overall dimensions of the test bench together with the relevant dimensions of some of the system components.

Description	Dimension [m]
Test bench width	1.30
Test bench depth	1.30
Test bench height	0.73
Aluminum disk diameter	1.10
Aluminum disk thickness	0.0185
Copper track inner diameter	0.88
Copper track outer diameter	1.00
Copper track thickness	0.015

Table 2.1: Test bench relevant dimensions.

2.2 Copper track characterization

The copper track consists of a circular crown with an internal diameter of 880 mm, an external diameter of 1000 mm and a thickness of 15 mm. It is bolted internally to the aluminium disc on which it rests and presents some non-idealities due to the positioning and the imperfect fixing. The modelling of these non-idealities is fundamental in the characterisation of the different parts that make up the test bench, as they can be decisive in conducting experimental tests.

A centesimal dial gauge with an accuracy of 0.001 mm is used to measure the height of the copper track with respect to a common reference, data are collected for 36 points along the circumference of the track (approximately every 10 degrees) and every 10 mm starting from the inner diameter and moving in a radial direction. The characterisation setup and measurement points are clarified in the pictures below.

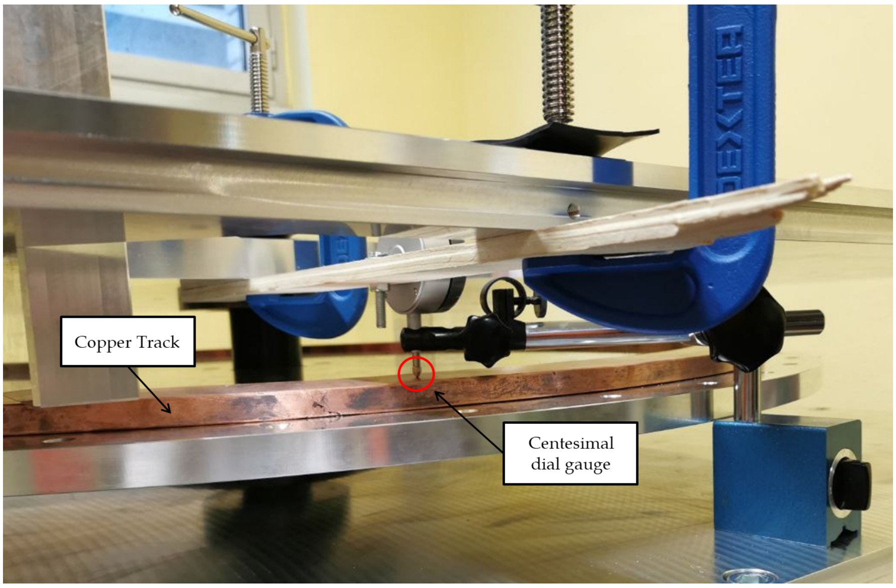

Figure 2.2: Copper track characterization setup.

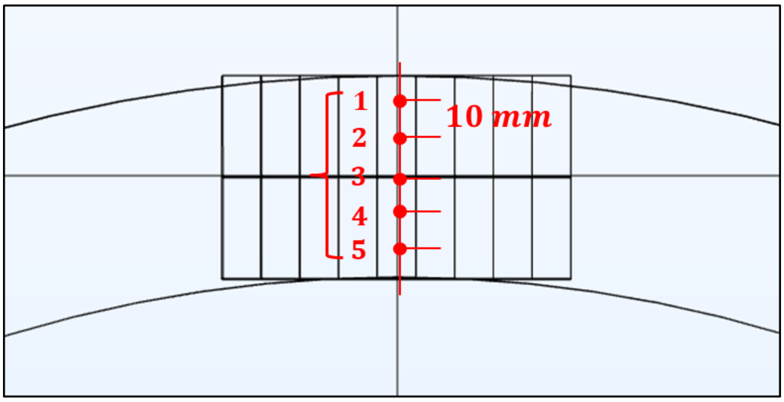

Figure 2.3: Characterization's measurement points.

The results of the characterisation are shown below. Different lines of the graph represent different measuring circumferences at an increasing distance from the inner diameter of the copper track.

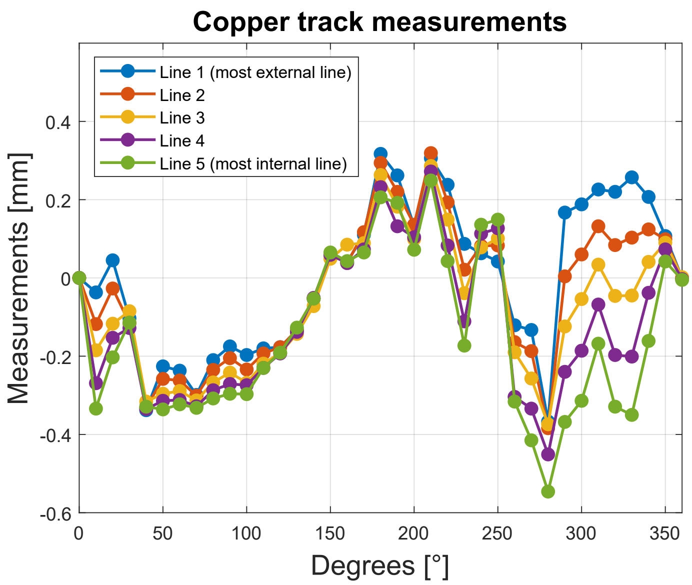

Figure 2.4: Copper track characterisation's measurements.

The first measurement point is taken as a reference corresponding to 0 degrees and its height, measured with the centesimal dial gauge, is set as a 0 mm reference. It can be observed from the experimental results that the overall height of the copper track varies from a minimum of -0.546 mm (in the innermost part of the track, line 5) to a maximum of 0.319 mm (in the part towards the outside of the track, line 2) for a total deviation of 0.865 mm. A 3D representation of the copper track is shown in the figure below to further clarify the overall trend. The figure is not in scale, but is reported as a qualitative realisation of the measured experimental data. The grey surface represents the 0 mm reference, while the numbered red dots refer to figure 2.3.

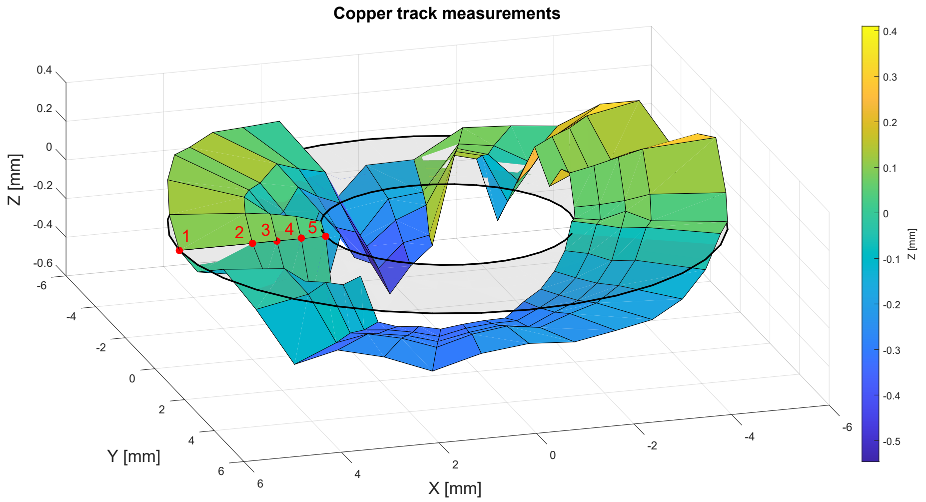

Figure 2.5: Copper track qualitative 3D representation.

2.3 Aluminum disk characterization

It is of fundamental importance to characterise the aluminium disc on which the copper track is fixed, following procedures similar to those described in the previous section. The evaluation of possible eccentricities in the aluminium disc is essential, together with the characterisation of the copper track, to accurately evaluate the air gap between the copper track and the Halbach array of permanent magnets that constitutes the levitation system.

As in the previous section, a centesimal dial gauge is used, which is placed at about 10 mm from the outer diameter of the aluminium disc. Starting from a fixed initial point (aligned on the same radius of the initial measurement points for the characterisation of the copper track) which is taken as a reference at 0 mm, the deviation in height of 36 points, spaced of about 10 degrees along a circumference of the aluminium disc, is measured. The setup used for the test is shown below.

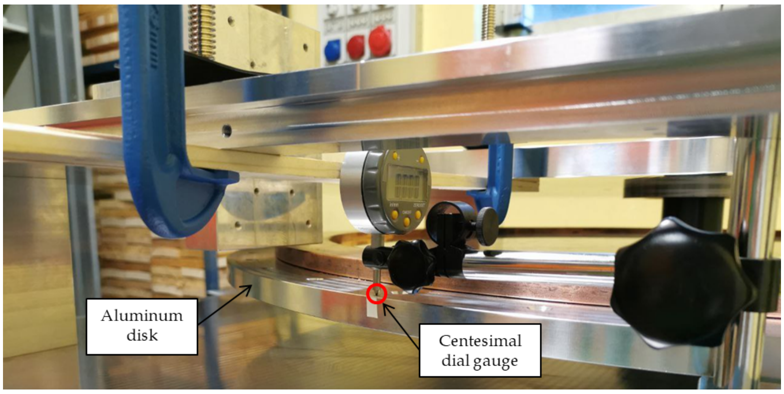

Figure 2.6: Aluminum disk's characterization setup.

The results of the measurements are shown in the graph below. The minimum point on this graph corresponds to a measured height of -0.028 mm and the maximum point to a height of 0.516 mm, resulting in a maximum deviation of 0.544 mm.

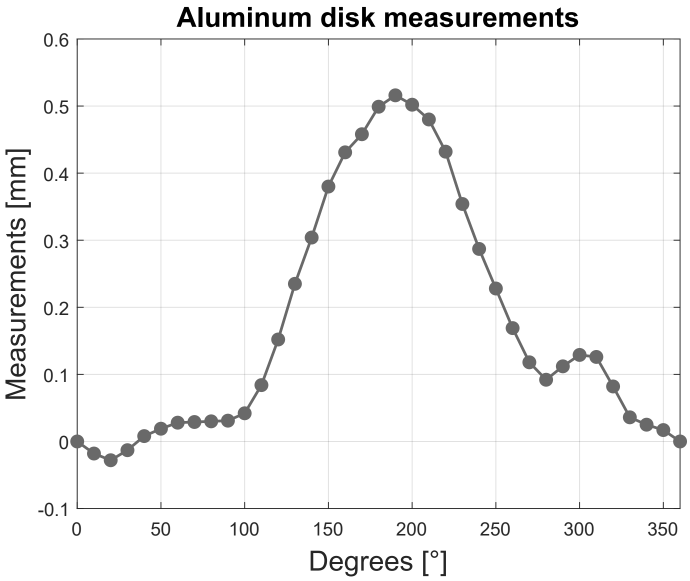

Figure 2.7: Aluminum disk's characterization measurement points.

Finally, a 3D representation of the measured deviations is shown in figure 2.8, with the aim of clarifying and emphasising the qualitative behaviour of the measurement points. The graph is not in scale, the proportions have been deliberately increased in order to obtain a comprehensible representation.

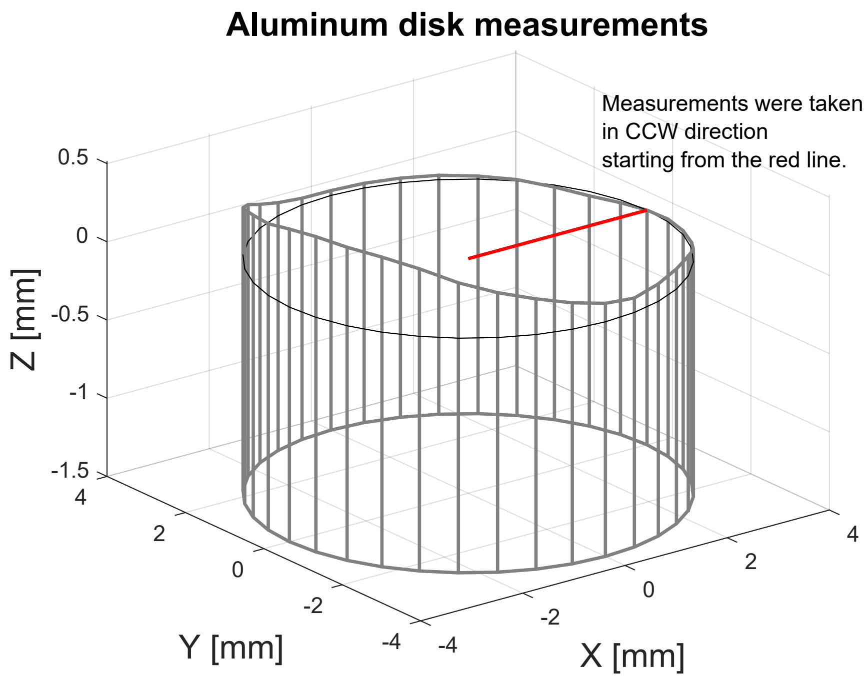

Figure 2.8: Aluminum disk's qualitative 3D representation.

2.4 Quasi static measurement stage

The quasi-static experimental tests to be conducted on the test bench aim at measuring the lift and drag forces (in the direction respectively perpendicular and parallel to the plane of the Halbach array) for different air gap values and for different copper track speeds. Figure 2.9 represents the 3D drawing of the measurement stage for conducting the quasi-static tests, the different parts making up the assembly are numbered to clarify the function of each of them.

The measurement stage is rigidly connected to the test bench by means of the connection plate n. 1. The vertical movement of the stage is allowed during the setup phase and is achieved by means of the micrometric linear stage n. 2 which allows to set with high precision the distance between the lower plane of the Halbach array and the copper track, i.e. the constant air gap.

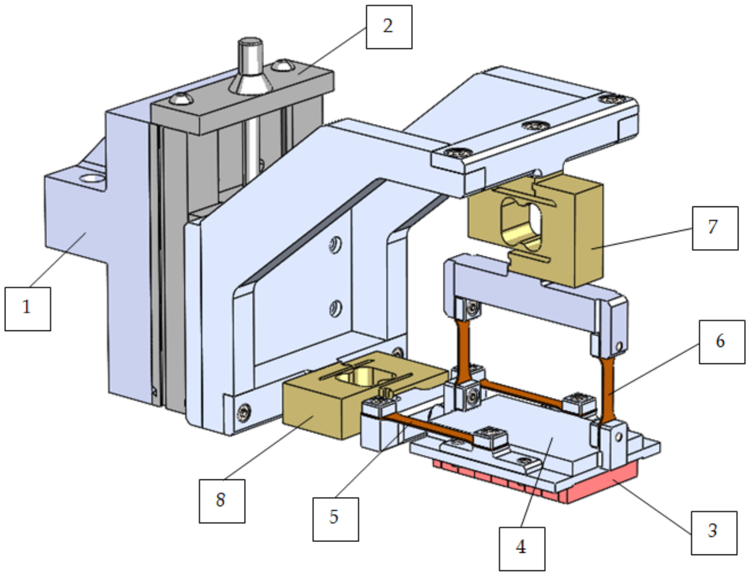

Figure 2.9: Quasi static measurement stage. Courtesy of Dr. A. Bonfitto, Eng. E.C. Zenerino and A. D'Oronzo.

Halbach array n. 3 is rigidly connected to aluminium pad n. 4, which allows the latter to be interfaced with the force measuring instruments. In particular, the system comprises two load cells (n. 7 and n. 8) positioned in two different planes and perpendicular to each other, which allow the measurement of lift and drag forces. The forces are transmitted from the aluminium pad to the load cells by means of flexure hinges that also involve the decoupling of the degrees of freedom.

N°	Component	N°	Component
1	Test bench connection plate	5	Horizontal flexure hinges
2	Micrometric linear stage	6	Vertical flexure hinges
3	Halbach array	7	Lift force load cell
4	Aluminum pad	8	Drag force load cell

Table 2.2: Quasi static measurement stage components.

2.4.1 Load cells characterization

The purpose of this subsection is to verify and quantify the accuracy of the force measurement of the load cells responsible for measuring lift and drag forces in the quasi-static configuration. Load cell 1 is the cell responsible for measuring the lift force in the direction normal to the plane of the Halbach array and the copper track. Load cell 2, on the other hand, is responsible for measuring the drag force in the direction parallel to the plane of the permanent magnet array and the track. The numbering of the load cells and the directions of the forces involved are clarified in the figure below.

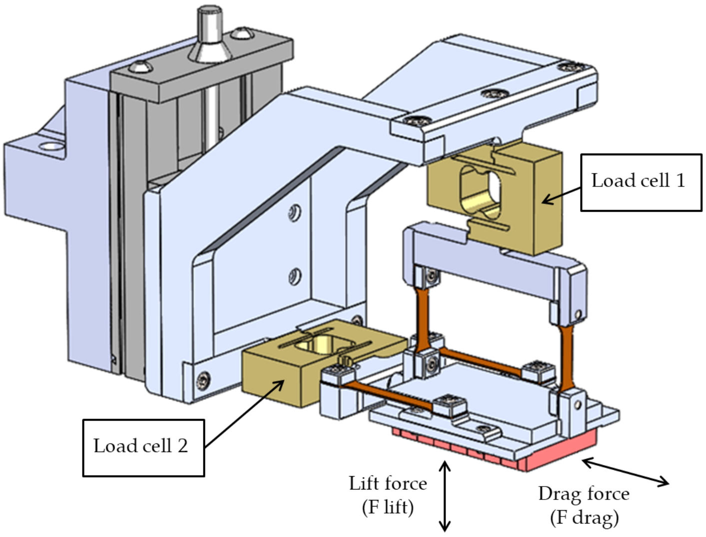

Figure 2.10: Load cells numbering and forces directions.

HBM S2M load cells have the possibility to measure variable forces in a range from 0 N up to 500 N with very high accuracy (see load cell datasheet in [1]). An HBM MGCPlus data acquisition system is used for conditioning and acquiring the signals coming from the load cells and provides the possibility of including additional modules. In particular, in the current setup, two ML55B one-channel amplifier plug-in modules are used (Datasheet in [33]).

Five different sample masses with five different force values are used to conduct the experimental test on the load cells. The mass and force values are shown in the table below.

[1] HBM S2M load cells datasheet: https://www.hbm.com/it/3364/s2m affidabilitrasduttori-di-forza-ad-s-di-alta-precisione/

Mass [Kg]	Force [N]
0.1300	1.27
0.6980	6.84
1.7610	17.26
3.0014	29.43
5.0026	49.05

Table 2.3: Sample masses and applied forces.

The five sample masses are applied directly to the load cells, keeping them independent of a particular configuration. The force values measured by the cells are recorded and compared with the actual force values exerted by the masses.

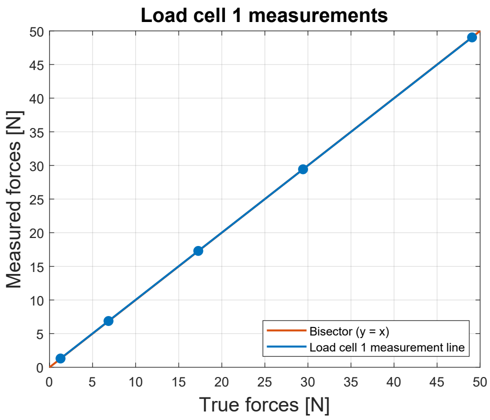

(a) Load cell 1 measurements.

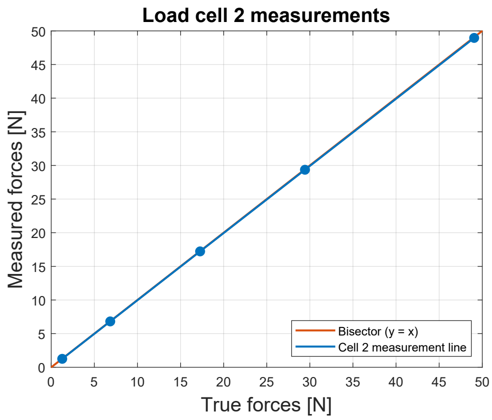

(b) Load cell 2 measurements.

Figure 2.11: Load cells measurements.

As can be seen from the graphs in figure 2.11, the load cells present a high accuracy in force measurements. The order of magnitude of the error committed by each load cell for each of the five measuring points is shown in the graphs below.

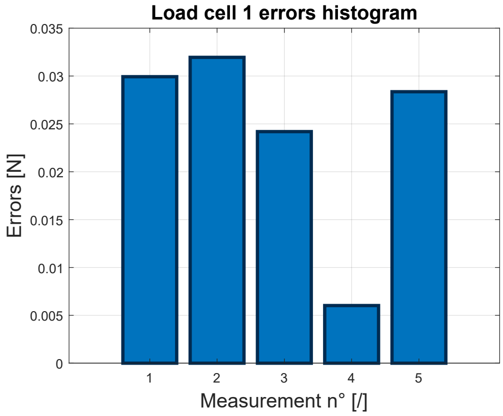

(a) Load cell 1 errors histogram.

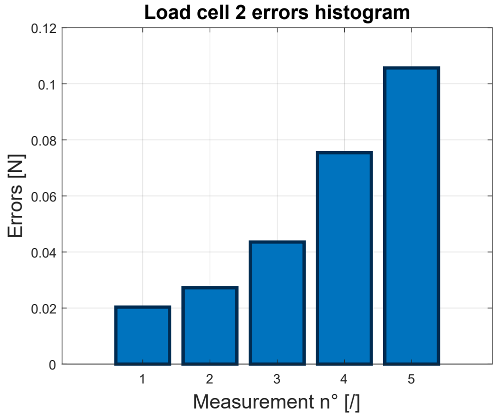

(b) Load cell 2 errors histogram.

Figure 2.12: Load cells errors histogram.

2.4.2 Load cells interference modeling

Load cells 1 and 2 are positioned in a perpendicular configuration to each other as can be seen in figure 2.10. This particular setup implies that when a force is applied parallel to the lift direction (cell 1), the load cell measuring the force in the drag direction (cell 2) will also be minimally affected by this force and will measure a value. The same observation can be repeated in the complementary configuration, when a force is applied parallel to the drag direction. The situation just described represents an undesired effect and it is important to model it in order to evaluate its entity and to implement possible correction strategies.

During the acquisition procedure, a load is applied in only one direction (lift or drag) and measurements from both load cells are acquired. The setup for both experimental tests is depicted in the following images. The aluminium plate which can be seen in figure 2.13a and 2.13b is used to separate the sample masses made of ferromagnetic material from the array of permanent magnets.

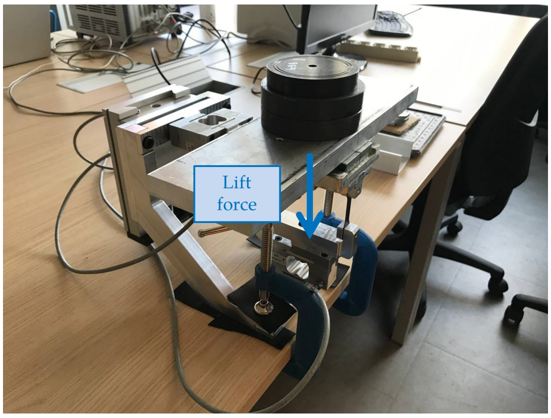

(a) Lift force application setup.

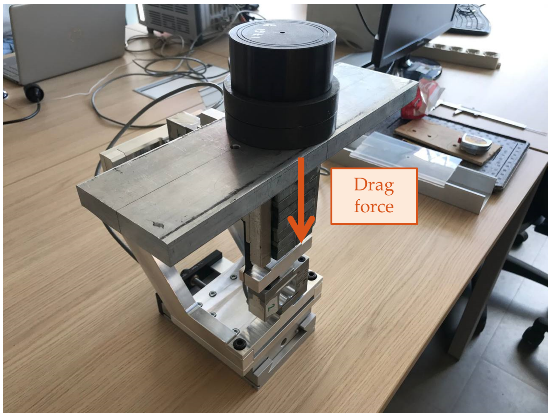

(b) Drag force application setup.

Figure 2.13: Load cells interference modeling setup.

Using ten sample masses in combination with each other, 17 different measuring points were chosen, which are shown in the following table.

Force measurement points [N]	**Force measurement points [N]**
1.27	26.46
3.84	29.43
5.19	33.27
8.11	36.27
9.81	39.24
13.65	43.08
17.26	46.70
19.62	49.05
23.46	

Table 2.4: Load cells interference measurement points.

The following graphs show the measurements taken on both load cells in the two configurations of lift force and drag force application. It can be seen that in the lift force application configuration load cell 1 measures force values close to those of the bisector, while load cell 2 measures force values close to zero. The same observation can be repeated in the drag force application configuration. The experimental results are shown in the graphs below.

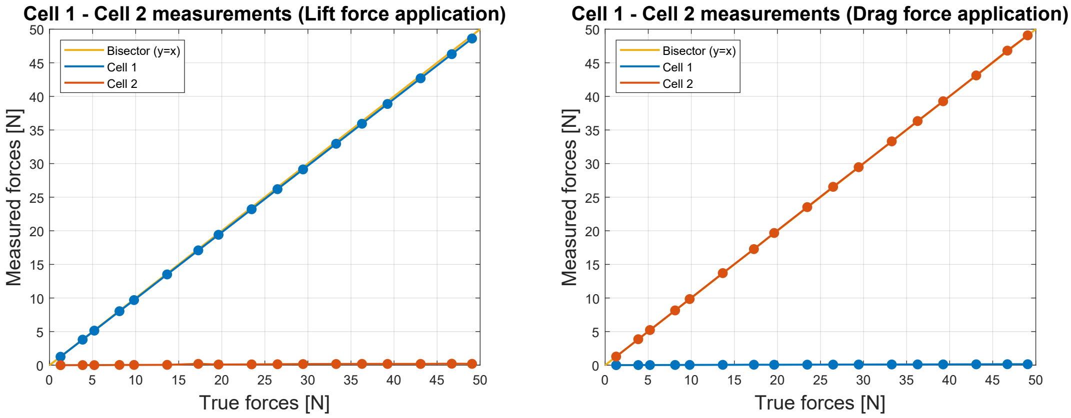

(a) Lift force application force measurements.

(b) Drag force application force measurements.

Figure 2.14: Load cells measurements.

The measurement points acquired on load cell 1 (in blue) and load cell 2 (in red) in both configurations of application of lift and drag forces were interpolated using a Curve Fitting algorithm in *Matlab* and four straight lines with respective values of angular coefficient and offset were obtained.

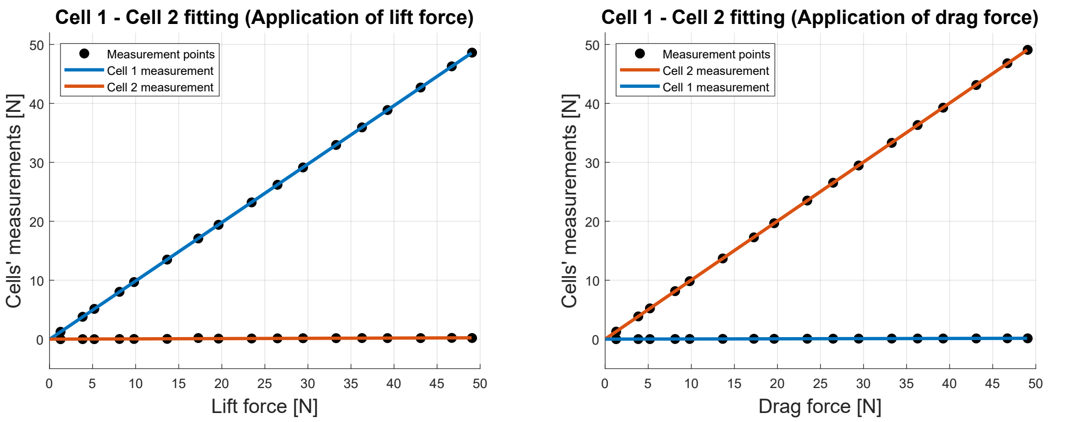

(a) Lift force application - fitting curves.

(b) Drag force application - fitting curves.

Figure 2.15: Load cells measurements.

The following is a zoom of the graph of figure 2.15a to clarify the distribution of the points to which the curve fitting algorithm is applied and the result that it allows us to obtain. Below, instead, the results obtained in terms of angular coefficient and offset for the four interpolating lines are reported in table 2.5.

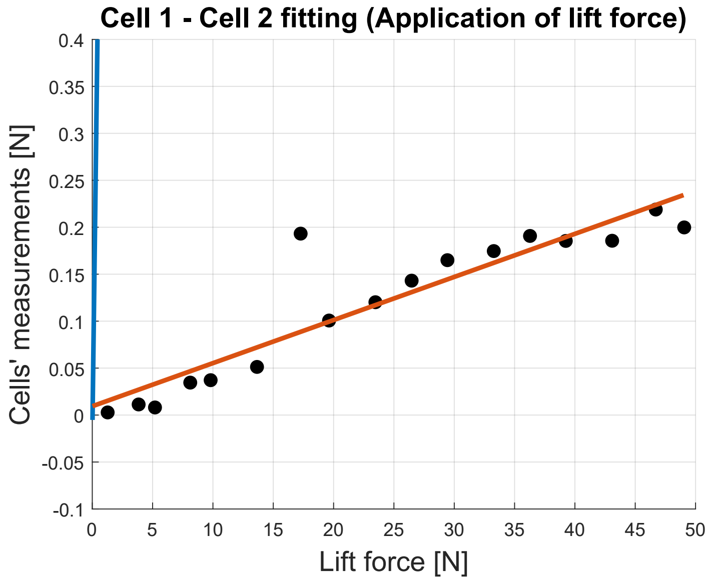

Figure 2.16: Cell 1 - Cell 2 (Application of lift force) - Zoom.

	Lift force application	Drag force application
Cell 1	$M1_{lift} = 0.9912$	$M1_{drag} = 0.0028$
Cell 1	$Q1_{lift} = -0.0241$	$Q1_{drag} = 0.0108$
Cell 2	$M2_{lift} = 0.0046$	$M2_{drag} = 1.0010$
Cell 2	$Q2_{lift} = 0.0094$	$Q2_{drag} = 0.0232$

Table 2.5: Curve fitting results.

The interference between the load cells can be modelled with the following equations:

$$\begin{cases} y_1 = M1_l x_l + M1_d x_d + Q1_l + Q1_d = M1_l x_l + M1_d x_d + Q1 \\ y_2 = M2_l x_l + M2_d x_d + Q2_l + Q2_d = M2_l x_l + M2_d x_d + Q2 \end{cases} \tag{2.1}$$

The force measured in the lift direction y_1 (measured by the load cell 1) is the sum of three different contributions: a contribution due to the force applied along the lift direction x_l, a contribution due to the force applied along the drag direction x_d and a contribution due to the offsets of the lines interpolating the measurement points (and related to the load cell 1), which add up to a single offset coefficient $Q1$. Similar reasoning can be applied regarding the force measured along the drag direction y2 (by the load cell 2).

The previous equations can be rearranged in matrix form:

$$\begin{bmatrix} y1 \\ y2 \end{bmatrix} = \begin{bmatrix} M1_l & M1_d \\ M2_l & M2_d \end{bmatrix} \begin{bmatrix} x_l \\ x_d \end{bmatrix} + \begin{bmatrix} Q1 \\ Q2 \end{bmatrix} \tag{2.2}$$

where:

- $Y = [2x1]$ - forces measured on load cell 1 ($y1$) and load cell 2 ($y2$).
- $X = [2x1]$ - theoretical forces applied on load cell 1 (x_l) and load cell 2 (x_d).
- $M = [2x2]$ - angular coefficients of the interpolating lineas
- $Q = [2x1]$ - offsets of the interpolating lines.

It is possible to derive the real applied forces x_l and x_d from the values of the forces measured in the two directions (lift and drag).

$$\begin{bmatrix} x_l \\ x_d \end{bmatrix} = \begin{bmatrix} M1_l & M1_d \\ M2_l & M2_d \end{bmatrix}^{-1} \left(\begin{bmatrix} y1 \\ y2 \end{bmatrix} - \begin{bmatrix} Q1 \\ Q2 \end{bmatrix} \right) \tag{2.3}$$

To clarify the concept behind the correction of the measured lift and drag forces, an example is given. Consider that a force is only applied in the direction of drag (direction of cell 2). In this case, theoretically, the force measured on load cell 1 should be zero (as represented in the graph below by the orange line). The measurement points are represented by the points in black, in blue the curve resulting from the fitting, while the values represented in green correspond to the force values resulting from the application of the correction matrices.

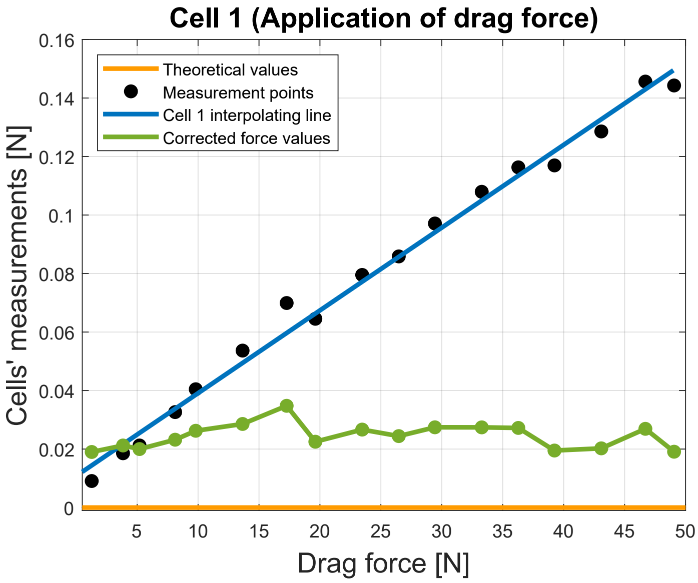

Figure 2.17: Cell 1 (Application of drag force) - Corrections.

Finally, the graph below shows the magnitude of the deviations between theoretical applied forces (null in this case) and the values of the measured forces before and after the application of the correction matrices. It can be observed that the error is drastically reduced.

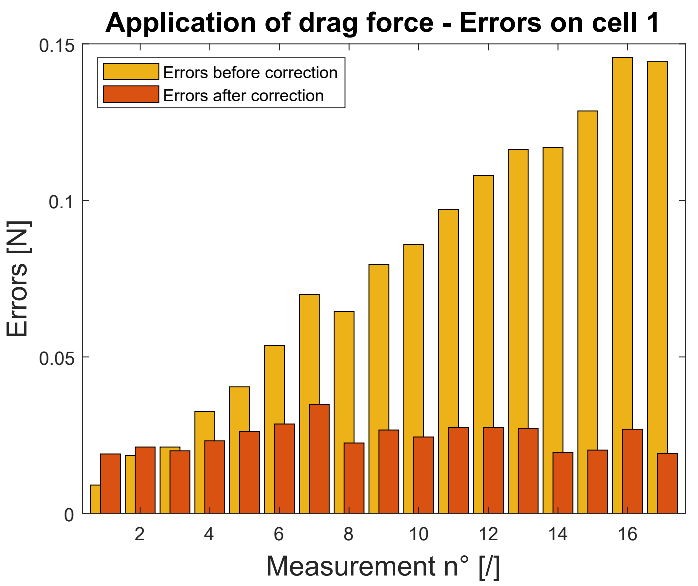

Figure 2.18: Cell 1 (Application of drag force) - Errors magnitude before and after correction.

2.5 Dynamic measurement stage

The objective of the dynamic tests is to evaluate the vertical dynamics of the system composed of two different masses, sprung and unsprung mass, which respectively represent the capsule and the bogie of a scale model of a Hyperloop train pod. The dynamic measurement stage is shown in two different views in figure 2.19.

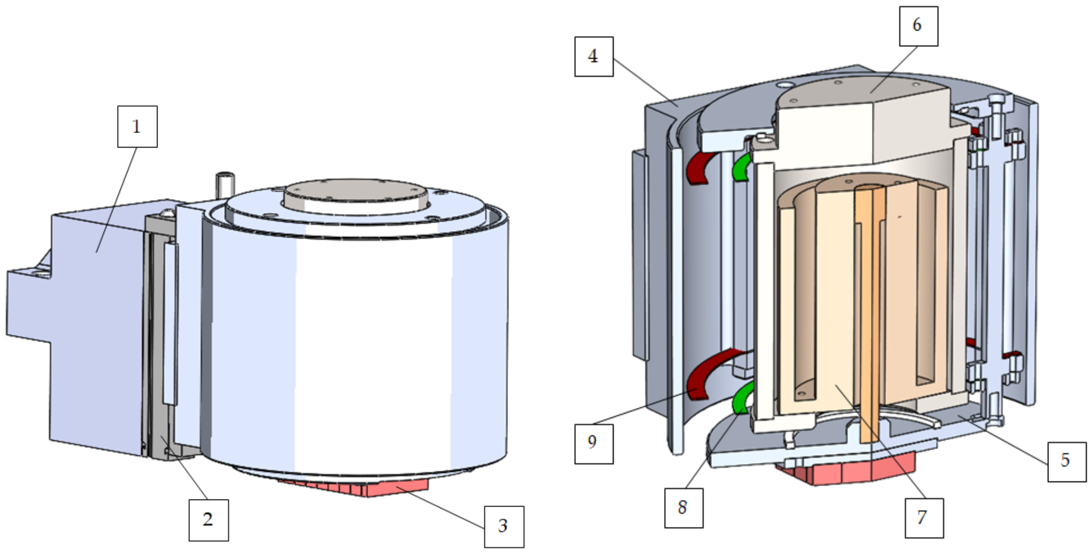

(a) 3D view. (b) 3D section view.

Figure 2.19: Dynamic measurement stage.

N°	Component
1	Test bench connection plate
2	Micrometric linear stage
3	Halbach array
4	Stator
5	Unsprung mass m_{us}

N°	Component
6	Sprung mass m_s
7	Voice coil Geeplus VM198-2P30
8	Unsprung - Sprung mass spring k_s
9	Stator - Unsprung mass spring k_{us}

Table 2.6: Dynamic measurement stage components.

The system can be represented as a quarter-car model to simplify visualisation and clarify the function of each component.

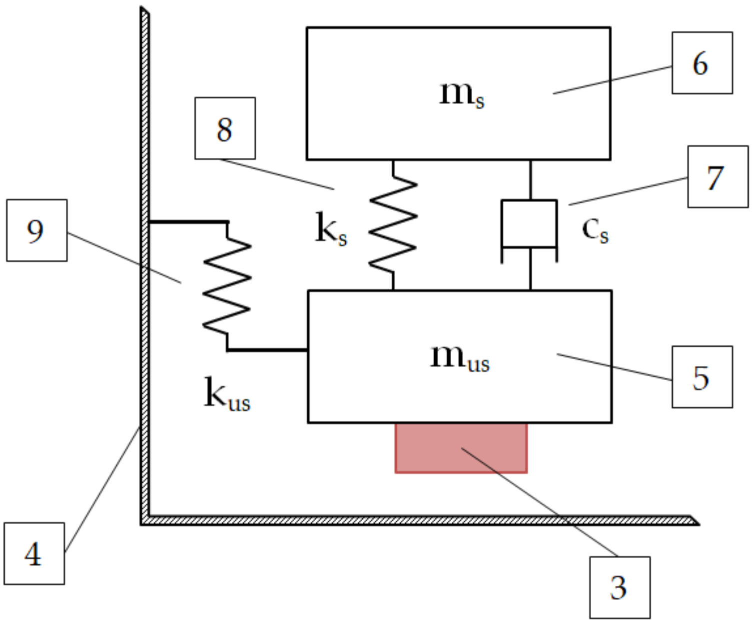

Figure 2.20: Quarter car model of the system.

The dynamic stage is rigidly connected to the test bench by means of the connection plate n. 1, while, as in the case of the quasi-static measurement stage, the micrometric linear stage n. 2 is used to set the initial air gap value. Stator n. 4 is connected to the micrometric linear stage and is fixed to it. The connection between the stator and the unsprung mass and between the unsprung and sprung mass is made by means of two rows of curved leaf springs, which have the function of preventing rotation and relative longitudinal displacement between the two masses. This results in a total of eight springs of stiffness k_{us} and eight springs of stiffness k_s, which are shown respectively in red and green colors in figure 2.19b. The secondary suspension between the two masses also comprises the voice coil n. 7 which can be controlled in order to introduce damping and improve the stability of the system. The moving shaft of the latter is integral with the unsprung mass m_{us}, while the main body comprising the permanent magnets and the coil is integral with the sprung mass m_s. Finally, as can be observed from both figures 2.19 and 2.20, the Halbach array n. 3 is rigidly connected to the unsprung mass m_{us}.

2.5.1 Springs characterization

The dynamic measurement stage is characterised by the presence of two springs, a first spring of total stiffness k_{us} interposed between the stator and the unsprung mass and a second spring of stiffness k_s interposed between the unsprung mass and the sprung mass, as it is possible to observe in the scheme of figure 2.20. In the real system, each of the springs represented as unique in the diagram is composed of eight curved leaf springs organised in two different layers, a lower and an upper one, which work in parallel to guarantee the necessary total stiffness. Each of them will have its own stiffness k which has to be evaluated with the aim of parameterising the system. Having the parts drawn using the modelling software *SolidWorks* and the information on the material that constitutes them, it is possible to carry out a finite element analysis (FEM) to evaluate the stiffnesses, using *SolidWorks Simulation* software.

Springs work mainly in bending, it is possible to consider one of the ends constrained by a fixed joint while the opposite end is left free to move by a carriage constraint. By applying a known force to the free moving end, the displacements for each point of the spring are simulated and the stiffness is calculated. The results obtained from the FEM simulations for both types of springs are shown below, in the figure on the left the springs between stator and unsprung mass and in the figure on the right the springs between unsprung and sprung mass.

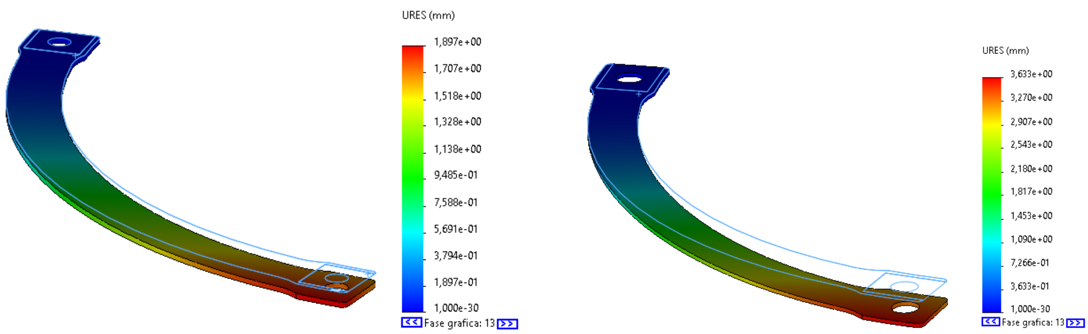

(a) Stator - Unsprung mass spring. (b) Unsprung mass - Sprung mass spring.

Figure 2.21: FEM simulations.

The spring stiffness can be calculated by considering the magnitude of the applied force and the maximum displacement, it can be written:

$$k_{us}\,(\text{single spring}) = \frac{F}{\Delta x} = \frac{1N}{1.897mm} = 0.527\frac{N}{mm} \tag{2.4}$$

$$k_{s}\,(\text{single spring}) = \frac{F}{\Delta x} = \frac{1N}{3.633mm} = 0.275\frac{N}{mm} \tag{2.5}$$

The eight springs of each type work in parallel and the stiffnesses are added together to obtain the total stiffness value:

$$k_{us} = 8 \times k_{us}\,(\text{single spring}) = 8 \times 0.527\frac{N}{mm} = 4.216\frac{N}{mm} \tag{2.6}$$

$$k_s = 8 \times k_s\,(\text{single spring}) = 8 \times 0.275\frac{N}{mm} = 2.2\frac{N}{mm} \tag{2.7}$$

2.6 Halbach array configuration

This thesis focuses solely on the description of a single Halbach array configuration, which has a particular arrangement of the magnetisation vectors of each permanent magnet. The results obtained and discussed in the following chapters will only refer to this particular configuration, and no other typologies will be discussed.

The configuration is composed by 9 permanent magnets with square cross-section of 12.7 x 12.7 mm and a length of 63.5 mm. The two magnets on either side of the configuration have a cross-section half that of the others, with rectangular dimensions of 12.7x6.35 mm. The magnetisation vectors are arranged at 45 degrees with respect to the vectors of the adjacent permanent magnets. The magnetisation pattern is shown in the figure below.

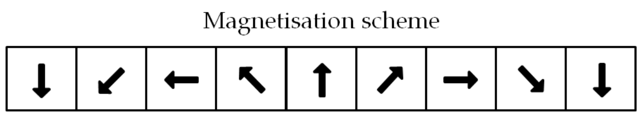

Figure 2.22: 45 degrees magnetisation Halbach array - Magnetisation scheme.

Below is a table containing some fundamental quantities useful for characterising the configuration taken into consideration.

Configuration	Feature	Symbol	Value
N45UH NdFeB PM Halbach array 45° magnetisation	Number of pole pairs	N_p	1
	Number of magnets per pole pair	N_m	8
	Magnet side length	a_m	12.7 mm
	Magnet in-plane depth	d_m	63.5 mm

Table 2.7: Halbach array's parameters.

The halbach array assembled with the aluminium pad for the conduction of quasi-static tests is shown in the figures below.

Figure 2.23: 45 degrees magnetisation Halbach array - Frontal view.

Figure 2.24: 45 degrees magnetisation Halbach array - Side view.

As can be seen from the figures above, the constructed and assembled permanent magnet array has some visible defects and some non-idealities such as imperfect centring in relation to the aluminium pad to which it is attached.

Chapter 3

Quasi static analysis

The aim of this chapter is to describe the experimental testing activities carried out on the test bench in the context of quasi-static analysis and the modelling and system identification activities with the objective of describing the levitation system with a multi-domain approach in the context of LTI systems. At first the theoretical background on which the analysis is based is described, then the experimental results of the quasi-static tests which are at the basis of the modelling and identification activities are presented and finally the LTI model which describes the levitation system together with the instability analysis following a root locus analysis approach is presented.

3.1 Theoretical background

3.1.1 System description

The levitation system bases its operating principle on the adoption of a Halbach array of permanent magnets rigidly connected to the aluminium pad at the base of the system and an electrically conductive copper track. The particular configuration in which the permanent magnets are arranged, as already described in the previous chapters, makes it possible to increase the magnetic field produced on one side of the array (the side that interfaces with the copper track) while it is attenuated on the opposite side. The rotation of the test bench and the relative speed between the magnet array and the copper track presupposes a variable magnetic field with respect to a metallic conductor, and thus the establishment of eddy currents within the latter by Faraday's Newmann Lenz law. A current induces a magnetic field that opposes the magnetic field that generated it, resulting in the establishment of lift and drag forces due to the interaction of the different magnetic fields involved.

The electromagnetic phenomena to which the permanent magnet array and the copper track are subjected can be described by the following equations:

$$\nabla \times H = J \tag{3.1}$$

$$J = \sigma (v \times B) \tag{3.2}$$

$$B = \mu_0 \mu_r H \tag{3.3}$$

Equation 3.1 is Maxwell's third equation, and represents the relationship between the magnetic field H and the current density J. Equations 3.2 and 3.3 represent, respectively, the contribution to the current density J due to the Lorentz force because of the relative movement of the parts and the relative velocity v, and Ampere's law describing the relationship between the magnetic field H and the magnetic flux density B.

3.1.2 RL lumped parameters model

The electrodynamic levitation phenomenon present an intrinsic non-linear nature and is characterised by a strong interaction between the electromagnetic domain, described in the previous subsection, and the mechanical domain. Pursuing the objective of simplifying the analysis, *Galluzzi et. Al* proposed an RL lumped parameters model that allows to characterize the electromagnetic domain and can be easily coupled with the mechanical domain.

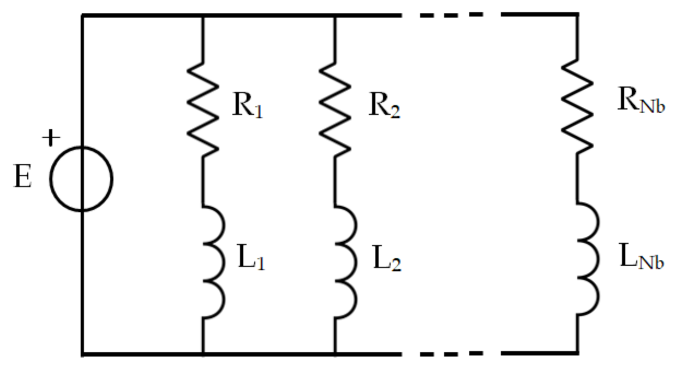

Figure 3.1: RL lumped parameters model scheme.

Figure 3.1 shows the RL lumped parameter model scheme. The model is characterised by a variable number of branches denoted by Nb, each consisting of a resistor and an inductor placed in series and indicated by R_{Nb} and L_{Nb}, respectively. A voltage generator closes the circuit. The dynamic behaviour of the eddy currents inside the copper track is modelled by electrically paralleling different branches characterised by specific resistance and inductance values that allow to discretize the density distribution of the currents flowing inside the track.

The relative motion between the permanent magnet array and the track results in a time varying megnetic flux linkage λ and the back-electromotive force contribution is taken into account within the RL model by means of the voltage generator E. For the k^{th} branch the circuit equation can be written as:

$$L_k \frac{di_k}{dt} + R_k i_k + E = 0 \tag{3.4}$$

with L_k and R_k the inductance and resistance of the k^{th} branch and i_k the current flowing in it.

By expressing the circuit in the phasor domain it is possible to calculate the power balance for each of the branches. By indicating with $i_{d,k}$ and $i_{q,k}$ respectively the direct (d) and quadrature (q) axis components of the current of the k^{th} branch it is possible to write:

$$L_k i_{\mathrm{d},k} \frac{\mathrm{d}i_{\mathrm{d},k}}{\mathrm{d}t} + L_k i_{\mathrm{q},k} \frac{\mathrm{d}i_{\mathrm{q},k}}{\mathrm{d}t} + R_k i_{\mathrm{d},k}^2 + R_k i_{\mathrm{q},k}^2 + E_{\mathrm{d}} i_{\mathrm{d},k} + E_{\mathrm{q}} i_{\mathrm{q},k} = 0 \tag{3.5}$$

The first pair of terms represents the rate of change of the stored magnetic energy. The second pair, instead, indicates the dissipated power by Joule effect. The last pair of terms represents the mechanical power developed by the levitation system, from which the lif and drag forces can be calculated. In static conditions, assuming constant vertical pad position z_{us} and constant longitudinal speed v is possible to solve for the direct and quadrature axis component currents and analytically compute the expressions of lift and drag forces as reported below:

$$F_{\mathrm{lift}} = \frac{\Lambda_0^2}{\gamma} \mathrm{e}^{-2z_{\mathrm{us}}/\gamma} \sum_{k=1}^{N_{\mathrm{b}}} \frac{\omega^2/\omega_{\mathrm{p},k}^2}{L_k \left(1 + \omega^2/\omega_{\mathrm{p},k}^2\right)} \tag{3.6}$$

$$F_{\mathrm{drag}} = \frac{\Lambda_0^2}{\gamma} \mathrm{e}^{-2z_{\mathrm{us}}/\gamma} \sum_{k=1}^{N_{\mathrm{b}}} \frac{\omega/\omega_{\mathrm{p},k}}{L_k \left(1 + \omega^2/\omega_{\mathrm{p},k}^2\right)} \tag{3.7}$$

The impedance of each of the branches in the circuit can be described through its electromagnetic pole frequency by:

$$\omega_{p,k} = \frac{R_k}{L_k} \tag{3.8}$$

3.2 Experimental setup and procedure

The experimental setup for conducting tests of quasi-static nature includes all those elements necessary to enable the test bench to be put into operation and in particular to set the aluminium disc and the copper track in rotation, and the elements that form the acquisition chain for monitoring the lift and drag forces that occur during operation.

A schematic representation of the setup is shown below.

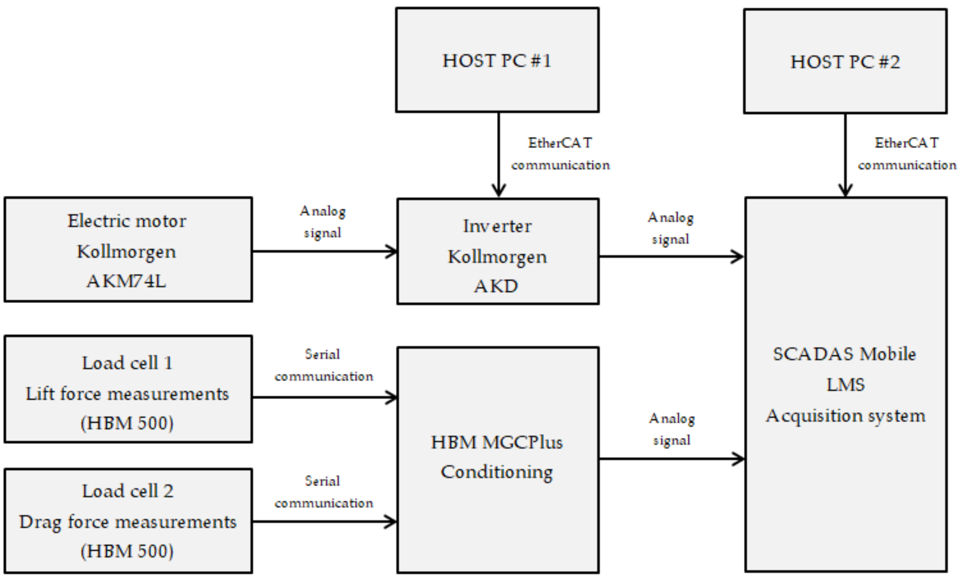

Figure 3.2: Quasi-static tests experimental setup scheme.

The Kollmorgen AKM74L electric motor is driven and controlled via a Kollmorgen AKD inverter and using the *Kollmorgen Workbench* program, which allows all electric motor operations to be managed. Host PC n. 1 can be used to set the angular speed to which the electric motor is to be driven and the characteristic parameters of the acceleration and deceleration phases. A resolver, an inductive displacement transducer, is used to monitor the angular speed, which is sent to the inverter via an analogue voltage signal. From the inverter, this signal is transmitted directly to the Scadas acquisition system, which takes care of the conditioning and acquisition of the angular speed signal. The analogue lift and drag force signals are transmitted via serial communication to the HBM MGCPlus conditioning system and then acquired via the Scadas acquisition system. Through host pc n. 2 it is therefore possible to acquire the lift and drag force signals and the angular velocity signal of the electric motor, and in turn of the aluminium disc and the copper track using *Simcenter TestLab Signature* program.

The actual experimental setup is shown below with an indication of its various elements.

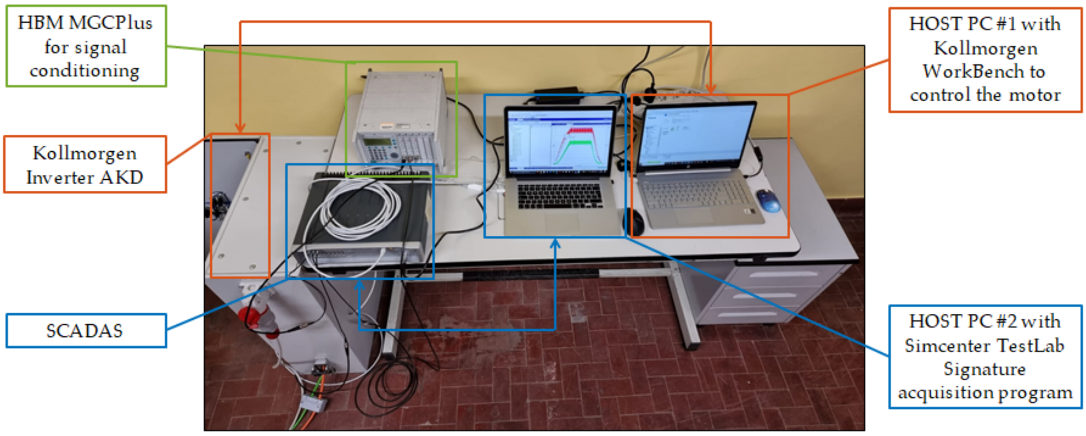

Figure 3.3: Quasi-static tests experimental setup.

The procedure followed in conducting quasi-static tests can be summarised in the following points:

- Setting distance between the Halbach array and the copper track, i.e. the airgap g.
- Setting the reference angular speed ω_{ref} of the rotor of the electric motor.

- Once the reference angular speed ω_{ref} has been reached and the time required for it to stabilise has elapsed, disable the inverter commuting so as to put the electric motor in a neutral state and let it decelerate due to the drag force and the inertia of the system.
- Acquisition of lift and drag force curves as a function of time.
- Repeat the above steps iteratively at different airgap g values.

3.3 Experimental results

3.3.1 Angular speed, lift and drag force profiles

The angular velocity profiles ω, measured in rpm, for different values of airgap g are shown in the graph below. Three different phases can be identified, which correspond to the acceleration phase in which the inverter drives the electric motor to reach the desired angular speed, a steady-state stabilisation phase in which the angular speed value is kept almost constant and a deceleration phase in which the power supply is cut off and the aluminium disc is left free to decelerate under the action of the drag force and inertia. The angular reference speed ω_{ref} for conducting quasi-static tests is set to 400 rpm. Considering the average radius of the copper track with respect to which the aluminium pad with the Halbach array is centered $r = 0.47\,m$, a maximum tangential velocity of $19.69\,m/s$ is obtained.

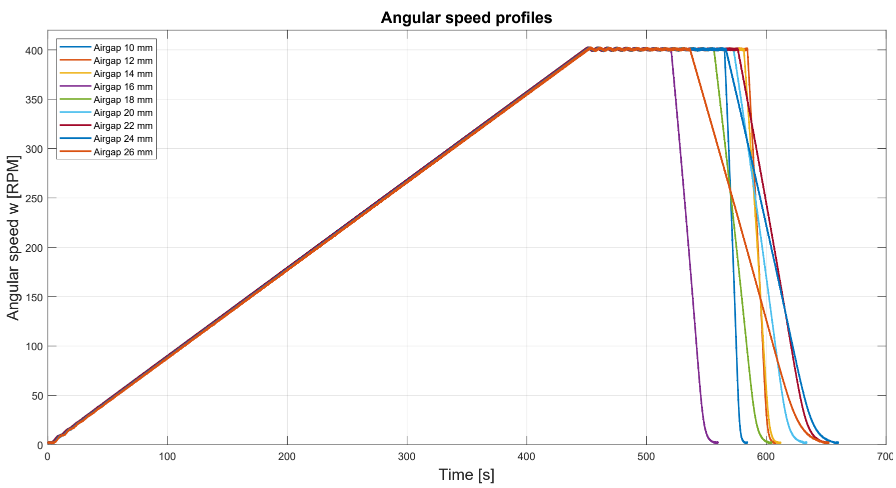

Figure 3.4: Augular speed profiles for different airgap g values.

Lift force and drag force profiles are acquired throughout the experiment, during all three phases and are reported below. As can be seen from the drag force profile, the behaviour is not monotonic, but as the angular velocity increases, once the electromagnetic pole is passed, the drag force tends to decrease. A peak in the drag force profile can also be observed due to the fact that, once the deceleration phase of the aluminium disc has started, the electromagnetic pole is passed again.

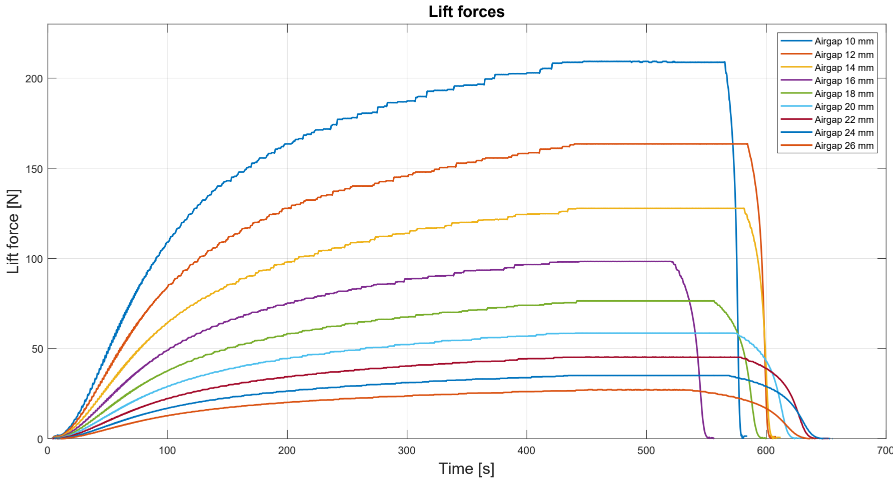

Figure 3.5: Lift forces profiles for different airgap g values as a function of time.

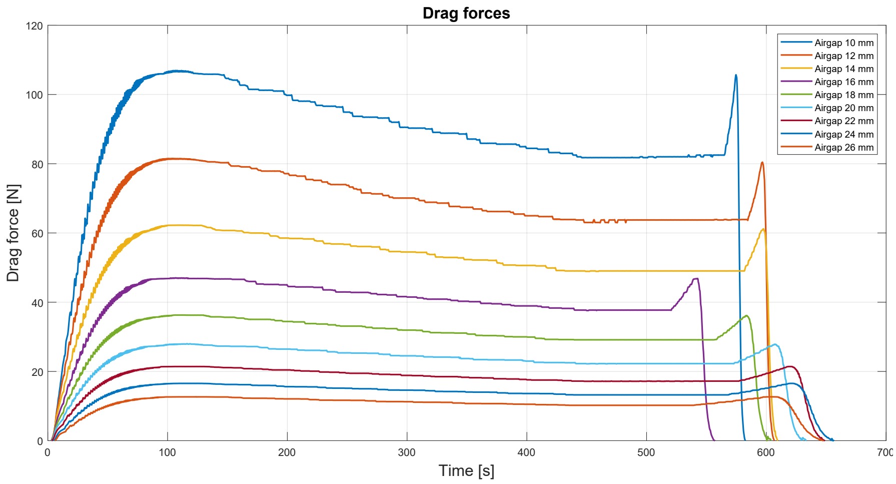

Figure 3.6: Drag forces profiles for different airgap g values as a function of time.

In order to express the trends of lift and drag forces as a function of the tangential speed of the copper track, only the deceleration phase of the system is taken into account. This is because during this phase the force contribution due to the work done by the electric motor is not present but only the forces of interest are considered.

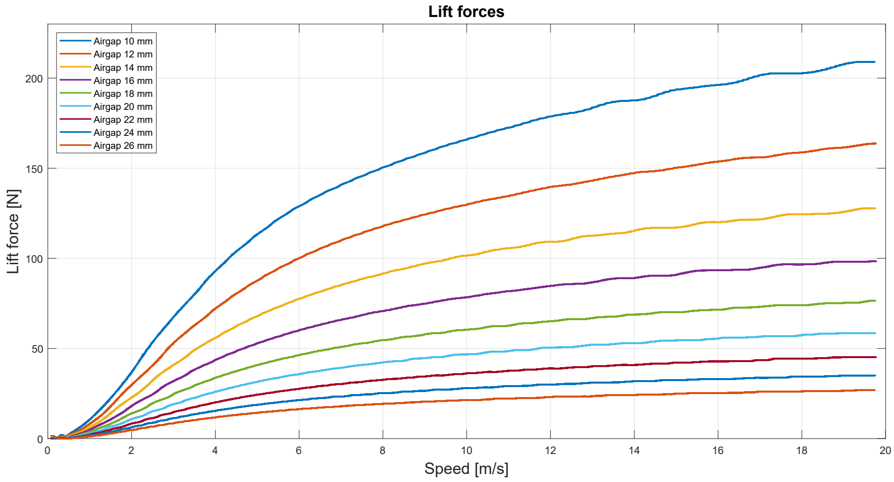

Figure 3.7: Lift forces profiles for different airgap g values as a function of speed.

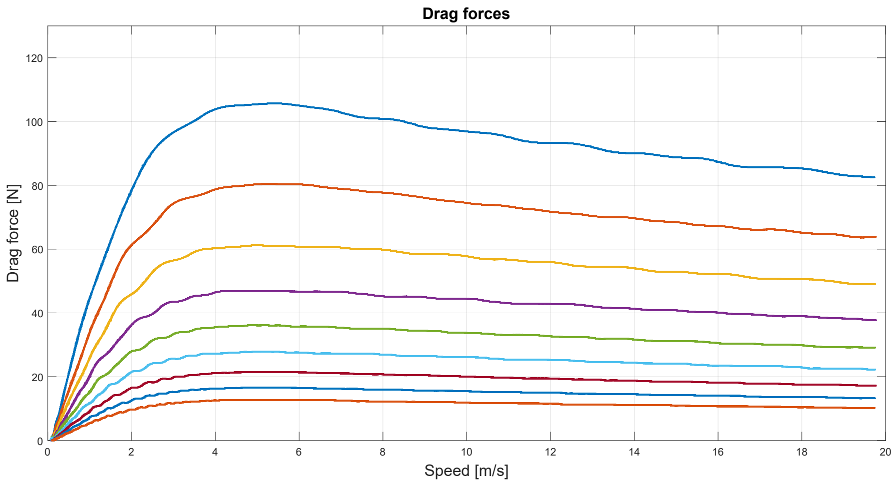

Figure 3.8: Drag forces profiles for different airgap g values as a function of speed.

As already noted above, the presence of the electromagnetic pole, beyond which the drag force begins to decrease with increasing tangential velocity, can also be observed in figure 3.8.

3.3.2 Lift to drag ratio

It is of fundamental importance to evaluate the efficiency indices of the magnetic levitation system such as the ratio between the lift force obtained and the drag force generated as a function of the tangential speed. The lift to drag ratio is a measure of efficiency, the aim being to maximise the lift force in relation to the drag force.

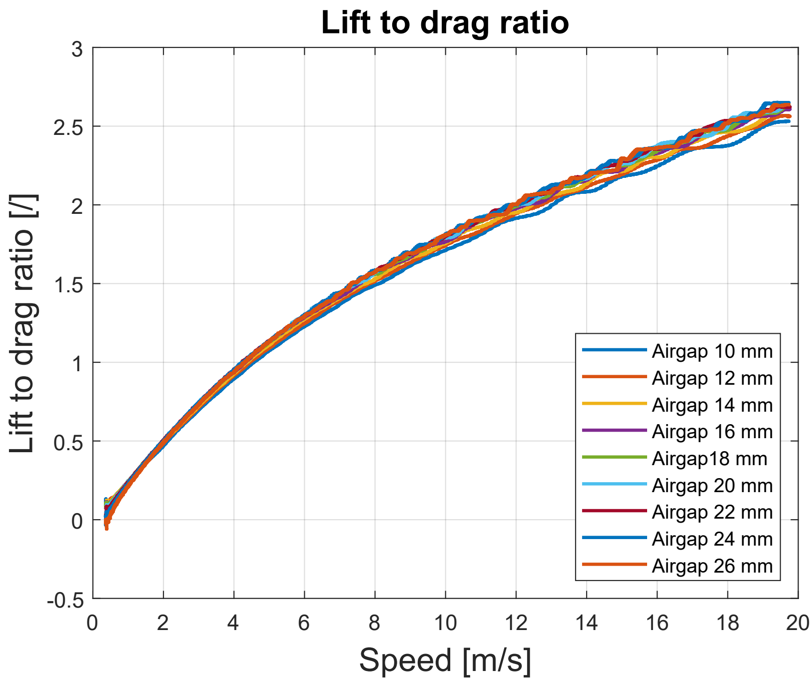

Figure 3.9: Lift to drag ratio.

In general, as the tangential speed increases, there is an increase in the lift to drag ratio. This is due to several factors. Firstly, as the tangential speed increases, the increase in lift force and drag force are not equivalent, but the former increases more in terms of absolute value. In addition, once the electromagnetic pole is passed, the drag force decreases with increasing tangential velocity, which leads to an increase in the lift to drag ratio.
For what concern the different airgap g values for which the experimental tests are conducted, a slightly lower efficiency is observed for lower airgap values. For example, at a tangential speed of 19 m/s (almost at the speed limit for which the system is tested) there is a decrease in the lift to drag ratio of 5.32% going from a maximum air gap value of 26 mm to a minimum value of 10 mm.

3.4 System identification for RL model parameters

As previously discussed in section 3.1.2, a linear RL lumped parameter model is introduced to analytically model the interaction between the Halbach array of permanent magnets and the copper track. Developing the analysis of the model in the phasor domain, two different equations describing the lift and drag forces as a function of the circuit parameters are obtained (the equations have been introduced before and are given below for clarity of content):

$$\begin{aligned}\bar{F}_{\text{lift}} &= \frac{\Lambda_0^2}{\gamma} \mathrm{e}^{-2z_{\mathrm{p}}/\gamma} \sum_{k=1}^{N_{\mathrm{b}}} \frac{\omega^2/\omega_{\mathrm{p},k}^2}{L_k\left(1+\omega^2/\omega_{\mathrm{p},k}^2\right)} \\ \bar{F}_{\text{drag}} &= \frac{\Lambda_0^2}{\gamma} \mathrm{e}^{-2z_{\mathrm{p}}/\gamma} \sum_{k=1}^{N_{\mathrm{b}}} \frac{\omega/\omega_{\mathrm{p},k}}{L_k\left(1+\omega^2/\omega_{\mathrm{p},k}^2\right)}\end{aligned}$$

The experimental data collected and presented in the previous section are used to identify the resistance R_k and inductance L_k parameters for each branch of the RL circuit, for a variable number of branches N_b to be optimised. The data are fitted into the equations above with the aim of minimising the l_2 norm between the actually measured lift and drag force values and the force values estimated by the model. The errors made can be indicated as $\Delta_L = \bar{F}_L - F_L$ for the error on the lift force and $\Delta_D = \bar{F}_D - F_D$ for the error on the lift force, where $\bar{F}_L$, $\bar{F}_D$ indicate the force values estimated by the model while F_L, F_D the experimentally measured force values.

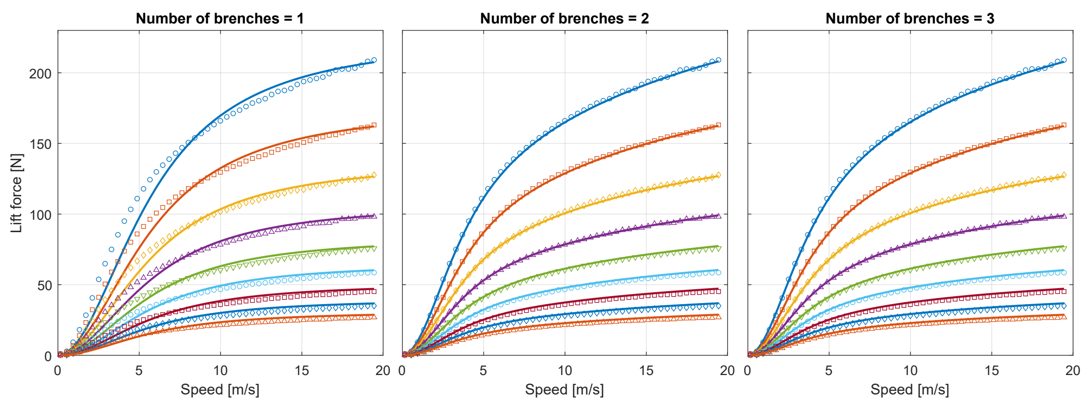

Figure 3.10: Experimentally measured lift forces Vs RL model estimated lift forces as a function of the number of brenches N_b.

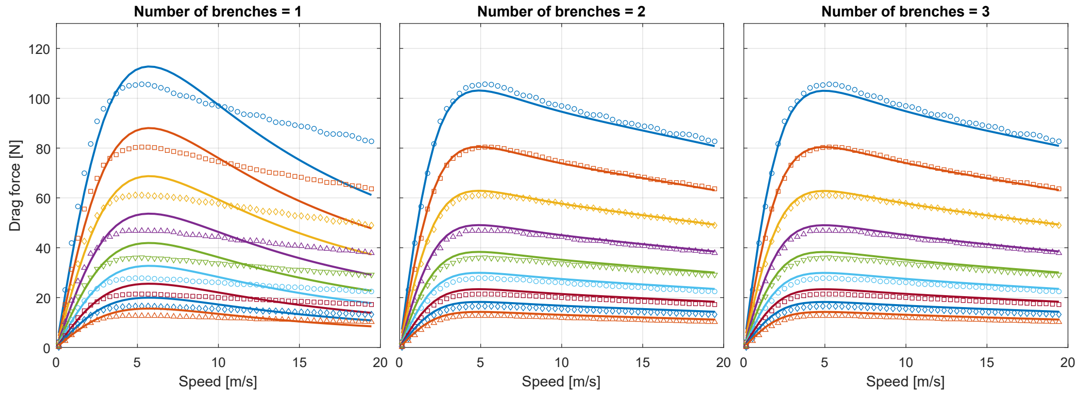

Figure 3.11: Experimentally measured drag forces Vs RL model estimated drag forces as a function of the number of brenches N_b.

Above are reported the behaviours of the experimentally measured lift and drag forces and the behaviours estimated by the RL model as a function of the tangential speed of the copper track and as a function of the number of branches N_b.
Considering only a single branch ($N_b = 1$), the fitting is highly inaccurate and the concentrated parameter RL model is unable to correctly approximate the trends in lift and drag forces. By adding a further branch ($N_b = 2$), the fitting is much more accurate than in the previous case. The estimation accuracy does not improve significantly by switching to a number of branches equal to 3. The graph below shows the fitting error as a function of the number of branches.

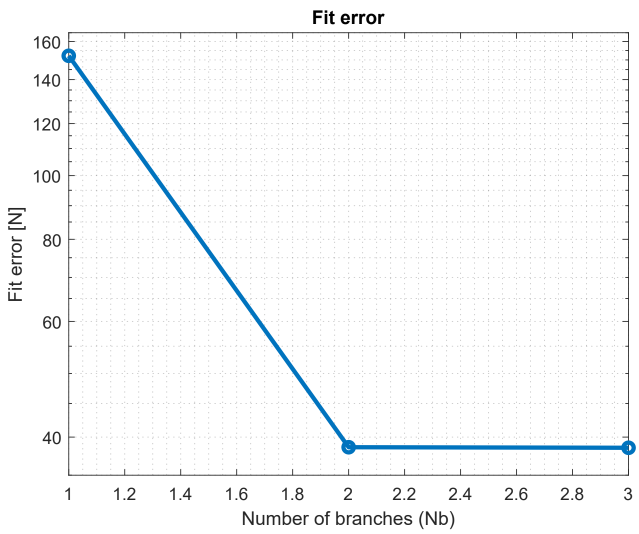

Figure 3.12: Fit error as a function of the number of brenches N_b.

Finally, the table below shows the values of the resistances R_k and inductances L_k as a function of the number of branches N_b of the RL model and the value of the fitting error already depicted in figure 3.12.

Number of branches $\mathbf{N_b}$	$\mathbf{N_b = 1}$	$\mathbf{N_b = 2}$	$\mathbf{N_b = 3}$
Resistances $\mathbf{R_k}$ [Ω]	$R_1 = 28.226$	$R_1 = 25.276$ $R_2 = 222.251$	$R_1 = 25.850$ $R_2 = 451.841$ $R_3 = 295.967$
Inductances $\mathbf{L_k}$ [H]	$L_1 = 0.080$	$L_1 = 0.108$ $L_2 = 0.180$	$L_1 = 0.114$ $L_2 = 0.733$ $L_3 = 0.210$
Fit Error [N]	152.18	38.61	38.53

Table 3.1: RL model's parameters and fit error as a function of the number of branches N_b.

It is necessary to ensure a good trade-off between accuracy of the RL model and computational performances. Observing a non-significant improvement in terms of fit error for a number of branches equal to 2 and at 3, $N_b = 2$ is chosen.

3.5 Root locus analysis

The linear RL lumped parameters model described in the previous sections makes it possible to couple the electromagnetic domain with the mechanical domain, and to study the dynamic evolution of the system with analysis tools such as root locus.

The mechanical domain is introduced into the analysis by modelling it through a quarter car model, as it is possible to observe in figure 2.20, consisting of two masses, a sprung mass and an unsprung mass, free to move in space, two springs, one of which is interposed between the two masses while the other between the unsprung mass and the stator, and a damper. Moreover, the system is also affected by the lift force that results from the interaction between the mechanical domain and the electromagnetic domain and is computed using the RL model. The equations representing the system simultaneously include the calculation of direct and quadrature currents in the phasor domain for each of the branches of the RL model, and the mechanical equations derived from the quarter car model. The equations are shown below:

$$
\begin{cases}
\frac{\mathrm{d}i_{\mathrm{d},k}}{\mathrm{d}t} = -\omega_{\mathrm{p},k} i_{\mathrm{d},k} + \omega i_{q,k} + \frac{\Lambda_0}{L_k \gamma} e^{-\frac{z_{us}}{\gamma}} \\
\\
\frac{\mathrm{d}i_{\mathrm{q},k}}{\mathrm{d}t} = -\omega_{\mathrm{p},k} i_{\mathrm{q},k} - \omega i_{\mathrm{d},k} - \frac{\Lambda_0}{L_k} \omega e^{-\frac{z_{us}}{\gamma}} \\
\\
\ddot{z}_{us} = \frac{F_{\mathrm{lift}}}{m_{us}} + \frac{c_s}{m_{us}} \left(\dot{z}_s - \dot{z}_{us} \right) + \frac{k_s}{m_{us}} z_s - \frac{k_s + k_{us}}{m_{us}} z_{us} - g \\
\\
\ddot{z}_s = -\frac{c_s}{m_s} \left(\dot{z}_s - \dot{z}_{us} \right) - \frac{k_s}{m_s} \left(z_s - z_{us} \right) - g
\end{cases}
\tag{3.9}
$$

The first two equations representing direct and quadrature currents $i_{d,k}$ and $i_{q,k}$ for each branch of the RL circuit can be linearised around a vertical displacement (airgap) of the unsprung mass $z_{us,0}$ as highlighted in the equations below:

$$
\frac{\mathrm{d}i_{\mathrm{d},k}}{\mathrm{d}t} = -\omega_{\mathrm{p},k} i_{\mathrm{d},k} + \omega i_{\mathrm{q},k} + \frac{\Lambda_0}{\gamma L_k} \mathrm{e}^{-z_{\mathrm{p},0}/\gamma} \dot{z}_{\mathrm{p}} \tag{3.10}
$$

$$
\frac{\mathrm{d}i_{\mathrm{q},k}}{\mathrm{d}t} = -\omega_{\mathrm{p},k} i_{\mathrm{q},k} - \omega i_{\mathrm{d},k} + \frac{\omega \Lambda_0}{\gamma L_k} \mathrm{e}^{-z_{\mathrm{p},0}/\gamma} \left(z_{\mathrm{p}} - z_{\mathrm{p},0} \right) - \frac{\omega \Lambda_0}{L_k} \mathrm{e}^{-z_{\mathrm{p},0}/\gamma} \tag{3.11}
$$

This makes it possible to use root locus as a tool for dynamic analysis. These relationships can be rearranged using a state space representation and a vector of states that includes direct and quadrature currents and accelerations of both sprung and unsprung masses:

$$
x = \{ i_{d,1} \quad i_{q,1} \quad i_{d,2} \quad i_{q,2} \quad \cdots \quad i_{d,N_b} \quad i_{q,N_b} \quad \dot{z}_{us} \quad z_{us} \quad \dot{z}_s \quad z_s \} \tag{3.12}
$$

From the state space representation, it is possible to extract the matrix A containing the fundamental eigenvalues for root locus analysis.

$$
A = \begin{bmatrix} \mathrm{A}_{\mathrm{el}} & \mathrm{A}_{\mathrm{ep}} \\ \mathrm{A}_{\mathrm{pe}} & \mathrm{A}_{\mathrm{m}} \end{bmatrix} \tag{3.13}
$$

$$\mathbf{A}_{\mathrm{el}} = \begin{bmatrix} -\omega_{p,1} & \omega & 0 & \dots & 0 & 0 \\ -\omega & -\omega_{p,1} & 0 & \dots & 0 & 0 \\ \vdots & \vdots & \vdots & \ddots & \vdots & \vdots \\ 0 & 0 & 0 & \dots & -\omega_{p,N_b} & \omega \\ 0 & 0 & 0 & \dots & -\omega & -\omega_{p,N_b} \end{bmatrix} \tag{3.14}$$

$$\mathbf{A_{ep}} = \begin{bmatrix} \frac{\Lambda_0}{\gamma L_1} e^{-z_{us,0}/\gamma} & 0 & 0 & 0 \\ 0 & \frac{\omega\Lambda_0}{\gamma L_1} e^{-z_{us,0}/\gamma} & 0 & 0 \\ \vdots & \vdots & \vdots & \vdots \\ \frac{\Lambda_0}{\gamma L_{Nb}} e^{-z_{us,0}/\gamma} & 0 & 0 & 0 \\ 0 & \frac{\omega\Lambda_0}{\gamma L_{Nb}} e^{-z_{us,0}/\gamma} & 0 & 0 \end{bmatrix} \tag{3.15}$$

$$\mathbf{A_{pe}} = \begin{bmatrix} -\frac{2\Lambda_0}{\gamma m_{us}} e^{-z_{us,0}/\gamma} & 0 & \dots & -\frac{2\Lambda_0}{\gamma m_{us}} e^{-z_{us,0}/\gamma} & 0 \\ 0 & 0 & \dots & 0 & 0 \\ 0 & 0 & \dots & 0 & 0 \\ 0 & 0 & \dots & 0 & 0 \end{bmatrix} \tag{3.16}$$

$$\mathbf{A_m} = \begin{bmatrix} -\frac{c_s}{m_{us}} & -\frac{k_s+k_{us}}{mus} & \frac{c_s}{m_{us}} & \frac{k_s}{m_{us}} \\ 1 & 0 & 0 & 0 \\ \frac{c_s}{m_s} & \frac{k_s}{ms} & -\frac{c_s}{m_s} & -\frac{k_s}{m_s} \\ 0 & 0 & 1 & 0 \end{bmatrix} \tag{3.17}$$

Mechanical domain parameters such as sprung and usprung masses, respectively m_s and m_{us}, and spring stiffnesses k_s and k_{us} were evaluated using *SolidWorks* modelling and simulation software, and are shown in table 3.2.

Parameter	**Symbol**	**Value**	**Units**
Unsprung mass	m_{us}	3.727	Kg
Sprung mass	m_s	16.451	Kg
Sprung - Unsprung mass spring	k_s	275	$\frac{N}{m}$
Unsprung mass - Stator spring	k_{us}	527	$\frac{N}{m}$

Table 3.2: Mechanical domain parameters.

In the root locus analysis, the system damping coefficient c_s is considered as a variable parameter.

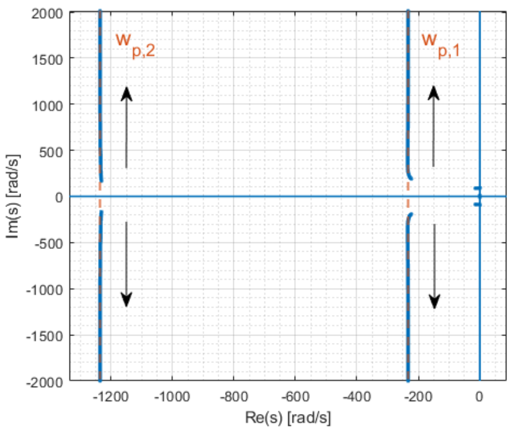

(a) Complete root locus.

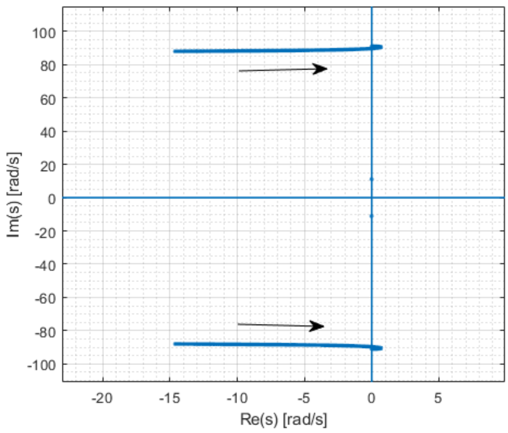

(b) Mechanical domain's zoom.

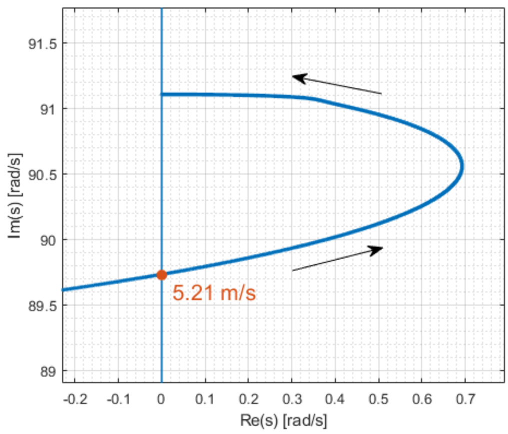

(c) Unsprung mass' zoom.

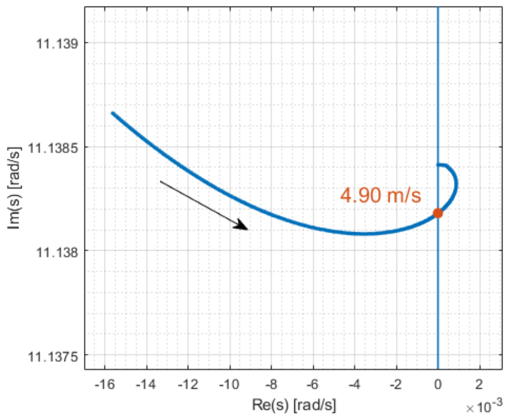

(d) Sprung mass' zoom.

Figure 3.13: Root loci of the system at increasing longitudinal speed (arrows), without suspension damping.

Without suspension damping, the quarter-car system exhibits the behavior that can be observed in figure 3.13. In the electromagnetic domain, the behaviour is asymptotically stable at $\omega_{p,1}$ and $\omega_{p,2}$. For the unsprung mass degree of freedom, the system has stable and complex poles at take off tangential velocity $2.68\,m/s$ with $s = -14.63 \pm 88.02i\,rad/s$. Similarly, for the sprung mass degree of freedom, the system has stable and complex poles at take off tangential velocity 2.68 m/s with $s = -0.0156 \pm 11.14i\ rad/s$. Instability is reached for the unsprung mass beyond 5.21 m/s, and beyond 4.90 m/s for the sprung mass. As can be observed in the figures above, the system present an unstable behaviour for a predominant part of the operating range, but it eventually tends to marginal stability as $v \to \infty$.

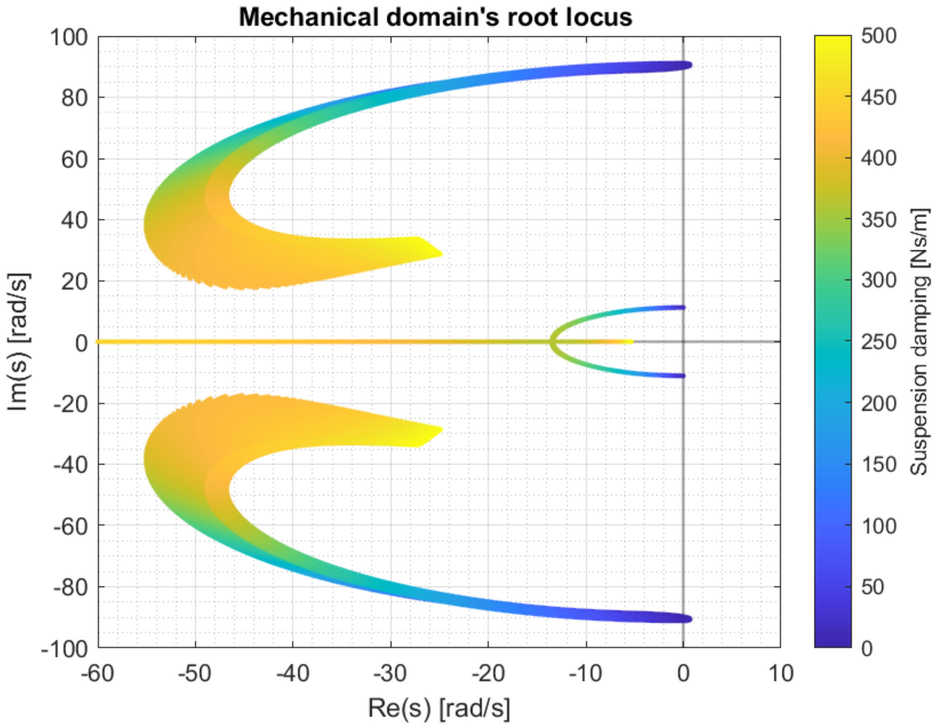

Figure 3.14: Fit error as a function of the number of brenches N_b.

Figure 3.14 shows the root locus regarding the poles of the mechanical domain and its evolution as a function of the suspension damping coefficient c_s, while figure 3.15 below shows the evolution of the pole with the largest real part as a function of the suspension damping coefficient and the behaviour of the damping ratio. This approach allows identifying the suspension damping value that maximizes the horizontal distance between the poles and the imaginary axis. The optimal suspension damping value that optimizes the system's stability is thus $c_{s,opt} = 362.73\ Ns/m$.

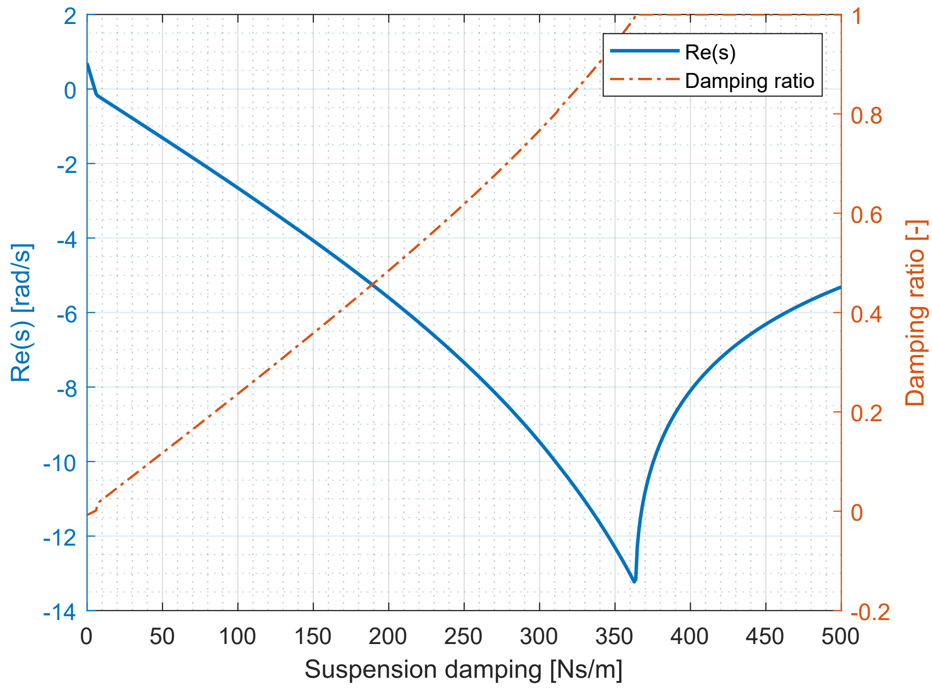

Figure 3.15: Optimal suspension damping $c_{s,opt}$ and damping ratio.

Chapter 4

Multibody simulations of different control strategies

The chapter deals with the multibody modelling of the dynamic stage using the *Matlab & Simulink* simulation program and in particular the *Simscape* and *Simscape Multibody* add-on and the subsequent simulation of different control strategies to add damping to the system and to ensure stability. Some of the different control techniques introduced in this chapter refer to F.Fanigliulo's master's thesis [30] and are treated and explained for the sake of clarity. A part of the chapter is also dedicated to the discussion of the secondary suspension used to stabilise the system, with a special focus on its operating principle and modelling.

4.0.1 Voice coil actuator

A voice coil actuator (VCA) is chosen as the secondary suspension for reasons of flexibility and control accuracy. Voice coil actuators, which are also known as a non-commutated DC linear actuators, are a typologie of direct drive linear motor. They consist of a statoric part made of ferromagnetic material, which allows the magnetic flux to be closed, and a movable part around which a copper coil is wound. Current can flow in both directions in the coil. The operating principle is based on Lorentz's law, according to which a conductor carrying a current and immersed in a magnetic field is subject to a force proportional to the intensity of the magnetic field, the current flowing in the conductor and the length of the latter. Permanent magnets, in a voice coil actuator, generate a radial magnetic field passing through the coil, which is affected by a force proportional to the current flowing through it and whose direction depends on the direction of the current:

$$F(t) = K_m i(t) \tag{4.1}$$

$$K_m = 2\pi BrN \tag{4.2}$$

where B is the magnetic field intensity, r is the average radius of the coil and N is the number of windings. A simplified scheme representing both the mechanical and electrical domains of a voice coil actuator is shown in figure 4.2.

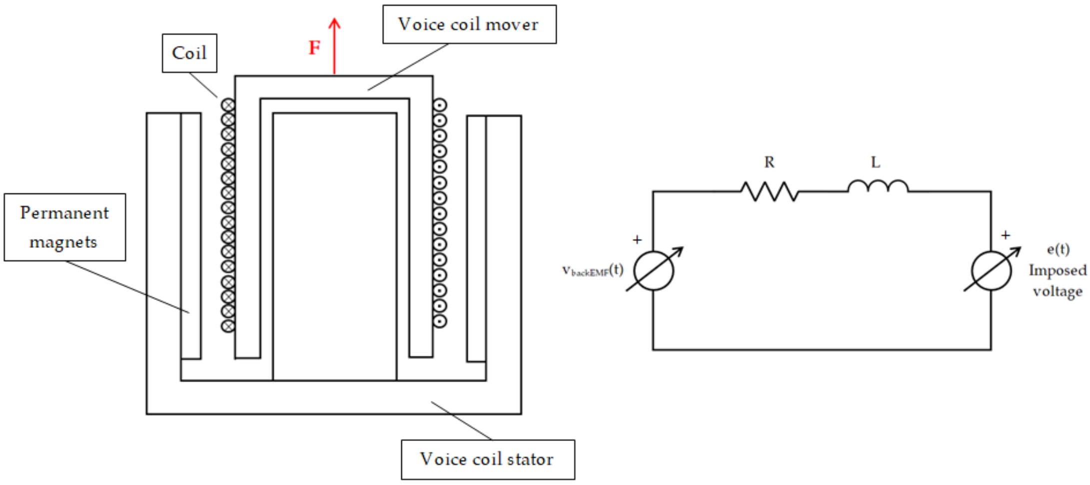

Figure 4.1: Voice coil actuator's scheme.

The electrical domain of a voice coil actuator can be modelled with a simple circuit characterised by a parasitic resistor R and inductance L, which in this case are considered as lumped parameters, and two ideal voltage generators. The first of these represents the externally imposed voltage required to drive the actuator and it is indicated by $e(t)$ in the scheme above, while the second ideal voltage generator is used to account for the voltage generated by the counter-electromotive force proportional to the speed of the voice coil mover and it is indicated by $v_{backEMF}(t)$. Note that this last element is necessary to link toghether the mechanical and electrical domains, in the same way as equation 4.1. From the circuit represented in figure 4.2 it is possible to write a Kirchhoff voltage low:

$$e(t) = L\frac{\mathrm{d}i(t)}{\mathrm{d}t} + Ri(t) + K_m v(t) \tag{4.3}$$

With regard to the physical implementation on the test bench, a voice coil actuator from the manufacturer *Geeplus*, model VM108-2P30-1000, was chosen. The main technical specifications of the actuator are given in the table below (the datasheet can be found in [34]).

Feature	Symbol	Value	Unit
Parasitic resistance	R	1.3	Ω
Parasitic inductance	L	N.A.	H
Force constant	K_m	25	N/A
Actuator's total mass	m_{TOT}	8	Kg
Coil mass	m_c	0.75	Kg
Peak force	F_{max}	230	N
Max output current	I_{max}	7.7	A

Table 4.1: VM108-2P30-1000 voice coil actuator, technical parameters.

A characterization procedure of the secondary suspension was conducted with the aim of identifying the resistance R and inductance L parameters, and it is possible to consult it within the thesis of the colleague Arianna Conchin Gubernati. The VCA was subjected to several step variations in the imposed voltage e(t) and current behaviours i(t) were recorded. During the experiment, the suspension coil is held in the fully retracted position, so as to keep the coils completely immersed within the magnetic field generated by the permanent magnets, and in such a way as to cancel the voltage contribution of the back electromotive force. The resulting circuit can be modeled as an RL circuit and the current behavior i(t) can be used to identify the R and L parameters by means of a fitting curve algorithm. The results obtained, considered in the remainder of the discussion, are shown in the table below:

Feature	Symbol	Value	Unit
Parasitic resistance	R	1.43	Ω
Parasitic inductance	L	11.1	mH

Table 4.2: VM108-2P30-1000 voice coil actuator, R and L identified parameters.

4.0.2 Dynamic measurement stage's modelling

Simscape Multibody is a multibody simulation environment dedicated to modelling 3D mechanical systems using blocks representing bodies, joints, constraints, force elements and sensors. It allows the development, simulation and testing of the performance of control systems that interact with hydraulic, electrical, pneumatic and other physical systems that can be modelled using Simscape add on. An important aspect to consider is the ability to integrate CAD geometries into the model, including masses, inertias, joints, constraints and 3D geometries developed using modelling environments such as *SolidWorks*. The modelling is based on a three-dimensional Cartesian coordinate system that allows the movements of the different parts that compose the system to be characterised, and its kinematic and dynamic evolution to be studied. *Simscape Multibody* also features the graphical visualization of the modelled system and its dynamic evolution through automatically generated 3D animations.

The dynamic measurement stage multibody's model is shown in figure 4.2.

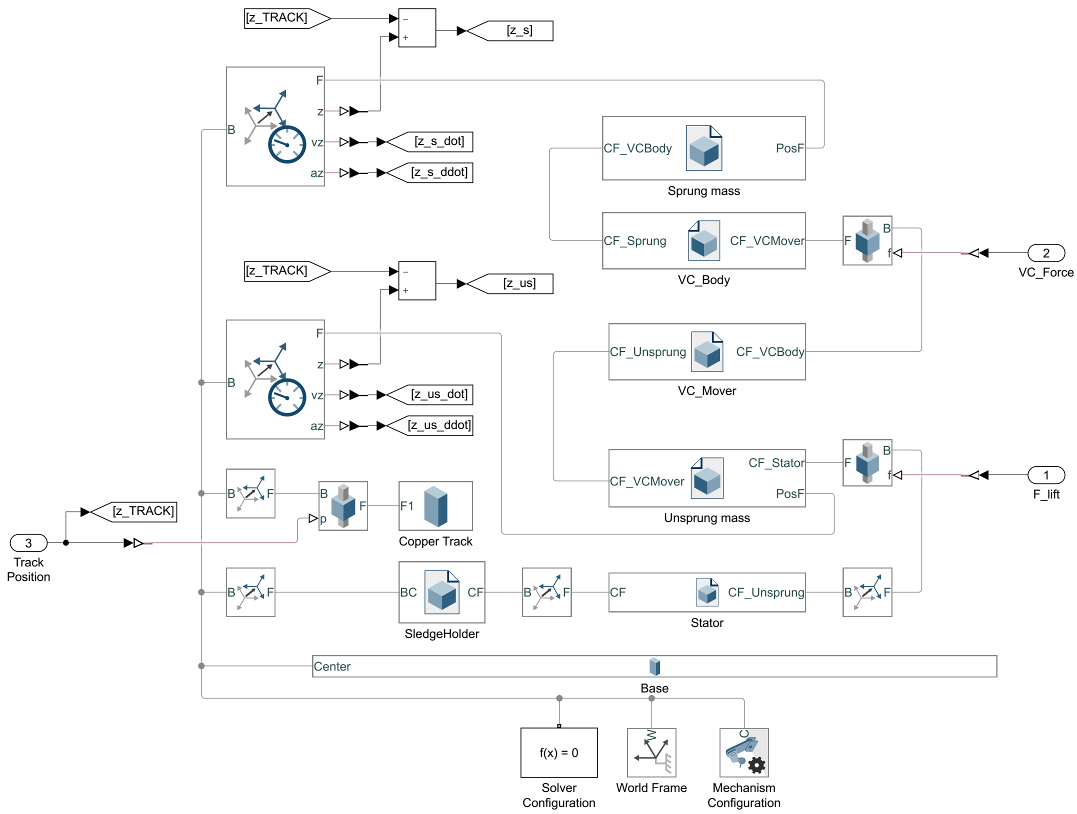

Figure 4.2: *Simscape Multibody* model of the mechanical domain of the dynamic measurement stage.

The system consists of five different parts. The stator is composed by a support plate, a linear micrometer stage that allows precision positioning of the entire dynamic measuring stage and a hollow cylindrical structure within which all other components that make up the system are positioned. The other components are the unsprung mass m_{us}, the sprung mass m_s and the secondary suspension represented by the voice coil actuator (VCA) described in the previous subsection, which is in turn divided into a body part (voice coil body) and a moving part (voice coil mover). The different components are introduced using the File Solid block and importing the geometries directly from the respective models in *SolidWorks*. Body movements and related constraints are defined by means of Prismatic Joint blocks, which also allow different types of actuation to be introduced. In this context, note that the different springs that compose the system are not directly included in the model because it is not possible to model circular springs within *Simscape Multibody*. The stiffnesses k_s and k_{us} introduced by the latter are included directly within the Prismatic Joint blocks and since the objective is to study the vertical dynamics of the system, the small differences in layout are not an element that can lead to discrepancies in the behaviour. The signals required for the implementation of the control systems can be acquired through the use of Transform Sensor blocks, which allow the recording of kinematic type signals such as position, speed and acceleration of the different components, and dynamic type signals such as the forces exchanged between them. A solid part representing the copper track is also present within the model, including the ability to raise or lower it with the aim of introducing disturbances within the control systems and testing their performance.

Two different views of the dynamic measurement stage are shown in the figures below.

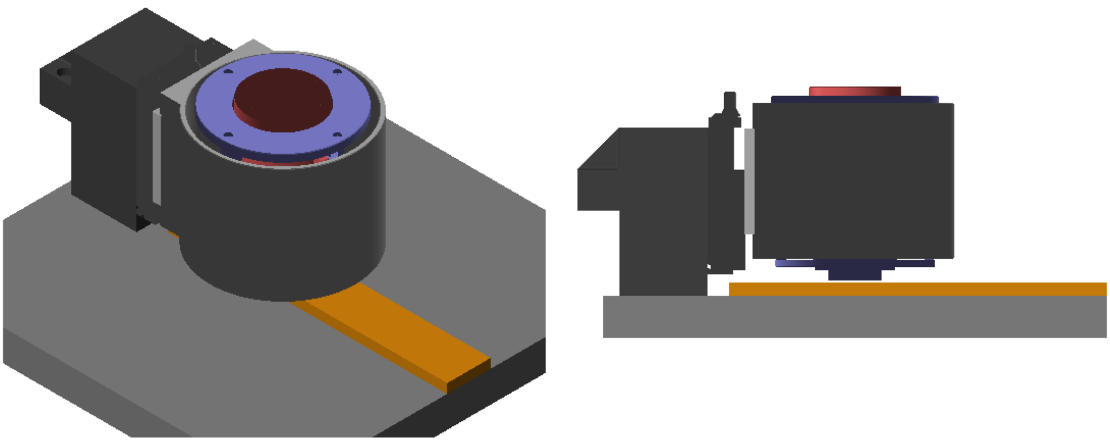

(a) Dynamic stage 3D view. (b) Dynamic stage front view.

Figure 4.3: *Simscape Multibody* model of the mechanical domain of the dynamic measurement stage, 3D representation.

The totality of the system is represented not only by the mechanical domain discussed above, but also by the electrical domain that is part of the secondary suspension subsystem. As discussed in the previous subsection, it is possible to model the electrical domain by means of an RL circuit with two ideal voltage generators and, in addition, it is possible to implement it directly in *Simulink* by means of the *Simscape* add on. The model of the electrical domain of the voice coil actuator is shown in the figure below:

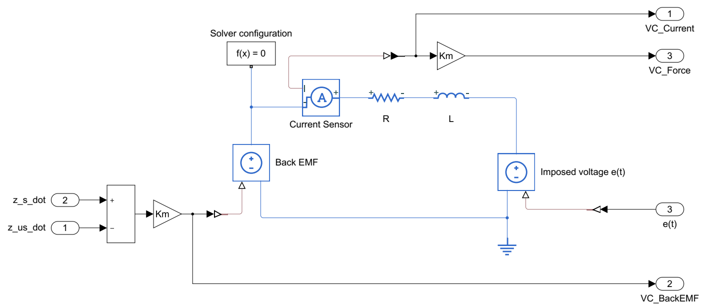

Figure 4.4: *Simscape* model of the electrical domain of the voice coil actuator.

Finally, the last subsystem of the model includes the calculation of the direct currents of the lumped-parameter RL model treated in Chapter 3 and the calculation of the lift force that excites the system. Since only the study of vertical dynamics is considered, the drag force is not taken into account. The position z_{us} and velocity $\dot{z}_{us}$ of the unsprung mass (Airgap and airgap variation, respectively), and the periodicity of excitation ω, which is derived directly from the desired tangential velocity profile of the copper track, are considered as system inputs.

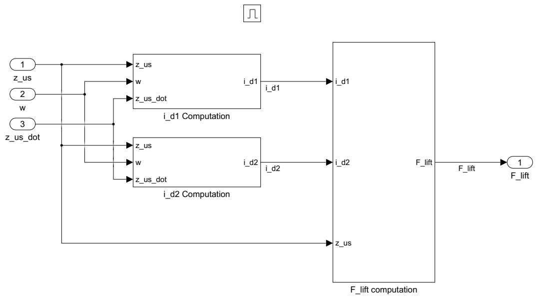

(a) Lift force computation subsystem.

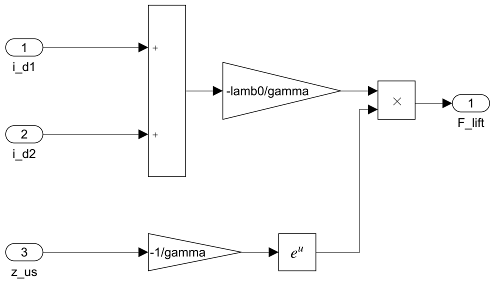

(b) Lift force computation block.

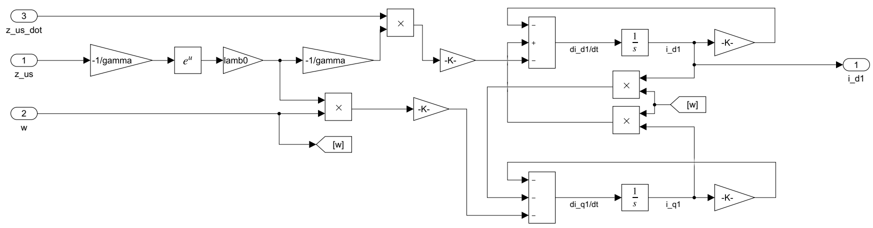

(c) Direct current computation block.

Figure 4.5: Lift force computation subsystem.

4.0.3 Instability observation

The root locus analysis conducted in Chapter 3 shows the occurrence of instability upon exceeding certain values of tangential velocity v of the copper track, which correspond to 4.90 m/s for the sprung mass m_s and 5.21 m/s for the unsprung mass m_{us}. Through multibody model simulation, it is possible to identify the behavior the system at different values of tangential velocity of the copper track and observe, for each of them, the occurrence or non-occurrence of instability. The RL circuit representing the electrical domain of the VCA is kept open circuited, as it is necessary to ensure zero damping force. The tangential velocity profile v of the copper track is shown in the figure below:

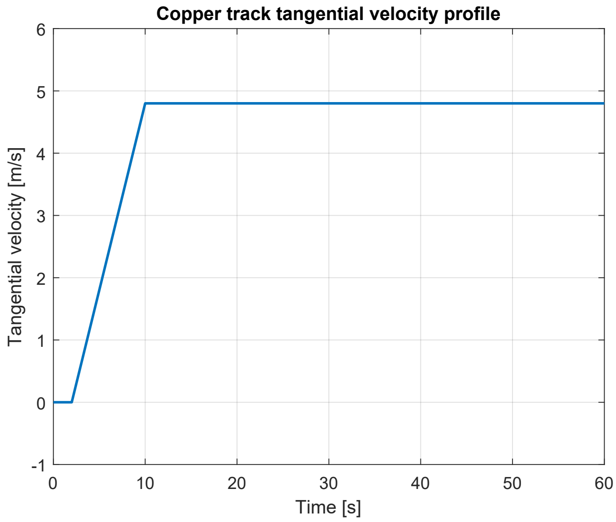

Figure 4.6: Tangential velocity profile v of the copper track.

Three different regions can be observed. An initial stabilization phase lasting $2s$ is introduced with the aim of allowing the masses to stabilize in their respective equilibrium positions. After that, an acceleration phase of the copper track from a zero tangential velocity to a target steady state velocity is identified, with a total duration of $8s$, from $t = 2s$ to $t = 10s$. Finally, a steady state phase in which the velocity is held constant, in order to better observe the behavior of the system in general and any insurgence of instability. It was chosen to simulate the system for steady-state tangential velocities of $v = 4.8\,m/s$ and $v = 5.3\,m/s$. The position of the unsprung and sprung masses with respect to the copper track for both cases are given below, in particular, the attention is focused on the steady state phase.

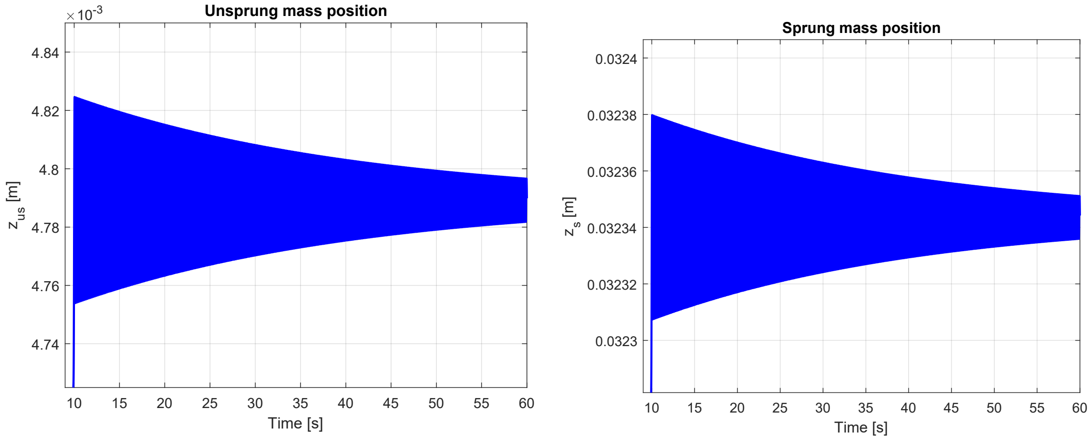

(a) Unsprung mass position. (b) Sprung mass position.

Figure 4.7: Unsprung and sprung mass position wrt copper track @ $v = 4.8\,m/s$.

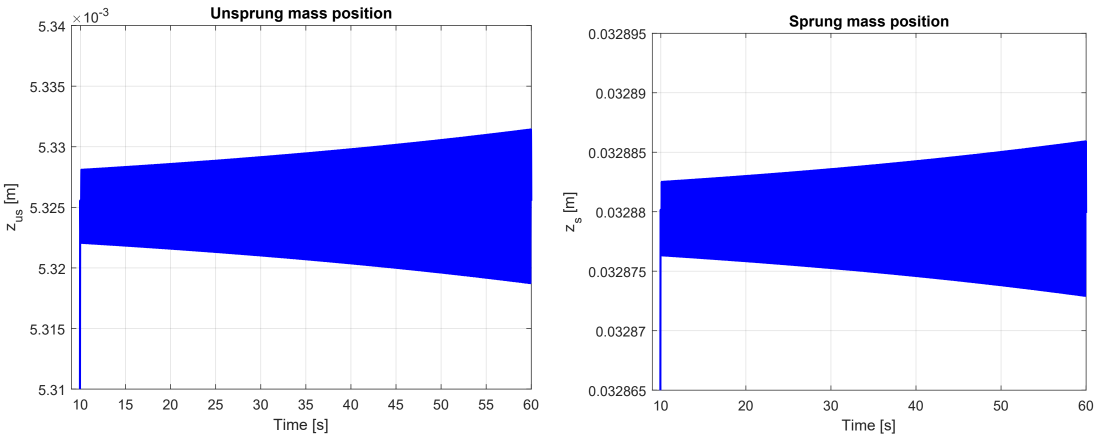

(a) Unsprung mass position. (b) Sprung mass position.

Figure 4.8: Unsprung and sprung mass position wrt copper track @ $v = 5.3\,m/s$.

From figures 4.7 and 4.8, it can be observed that for tangential velocities v of the copper track lower than the instability's velocities the oscillations decrease in time during the steady state phase, while for velocities higher than the instability's velocities, an increase in the amplitude of the oscillations is observed.

4.1 Control strategies

In this section, three different control strategies are introduced and the performance of each is tested and compared to the performances of the other control techniques with the aid of multibody simulations of the dynamic measurement stage.

4.1.1 Passive damping control with current feedback and feedforward weight compensation

This control strategy exploits the imposed voltage e(t), which is the driving voltage of the secondary suspension, as the control input. To understand how damping is introduced through the control system, the characteristic equations of the VCA 4.1 and 4.3 are given for the sake of completeness of exposition:

$$F(t) = K_m i(t)$$

$$e(t) = L\frac{\mathrm{d}i(t)}{\mathrm{d}t} + Ri(t) + K_m v(t)$$

Consider the imposed voltage $e(t) = -\alpha i(t)$ with $\alpha \in \mathbb{R}$. By substituting the first equation into the second and the control input definition, it is possible to write the expression of the damping coefficient by applying the Laplace transform (force-velocity transfer function):

$$c_{VC}(s) = \frac{F(s)}{v(s)} = -\frac{K_m^2}{sL + (R + \alpha)} \tag{4.4}$$

The real parameter α can be tuned to obtain a steady-state gain equal to c_{opt} as in the equation below:

$$\alpha \ \ s.t. \ \lim_{s\to 0}\left|\frac{F(s)}{v(s)}\right| = \frac{K_m^2}{R+\alpha} = c_{opt} \tag{4.5}$$

This is the first contribution to the control input, which allows damping to be introduced into the system. The definition of "Passive control" refers to the actual implementation of such a control, which can be achieved by placing in series with the VCA's electrical circuit a rheostat capable of varying the resistance of the latter and dissipating the power necessary to introduce the optimal damping.

A key point for each of the control strategies that will be introduced throughout the discussion concerns the compensation of the sprung mass weight. This is of paramount importance as it is necessary to ensure that the springs (with stiffness k_s) interposed between the sprung and unsprung masses operate within their linear region. To do this, it is necessary to provide a force equal in modulus and opposite in direction to the weight force of the sprung mass $P = m_s g$ by means of the secondary suspension, and this is equivalent to imposing a constant offset to the driving voltage e(t) on the VCA. It is possible to calculate this offset by writing a static equation for the RL circuit that models the electrical domain of the voice coil:

$$\begin{cases} e = (R + \alpha)i \\ F = Kmi \end{cases} \quad \rightarrow \quad e = \frac{F}{Km}(R + \alpha) = \frac{P}{Km}(R + \alpha) \tag{4.6}$$

Based on the linearization implemented and decribed in section 3.5, it is possible to consider the system as linear time-invariant (LTI), and therefore it is possible to apply the superposition principle to meet different requirements of a control strategy as separate contributions. Therefore, it is possible to write:

$$e(t) = -\alpha i(t) + \frac{m_s g}{Km}(R + \alpha) \tag{4.7}$$

The schematic of the control system architecture and the implementation in *Simulink* are depicted in the figure below.

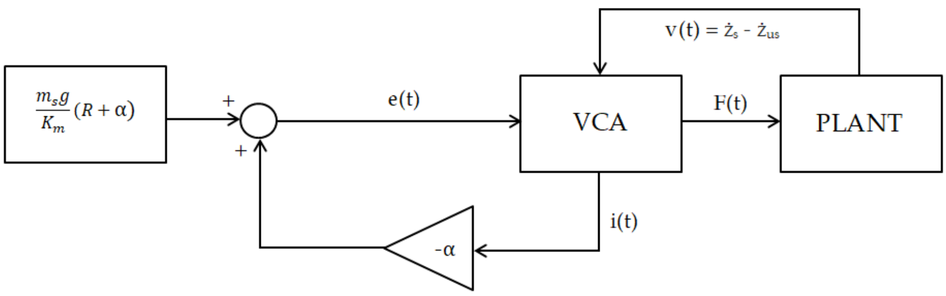

Figure 4.9: Passive damping control with current feedback and feedforward weight compensation, control system architecture.

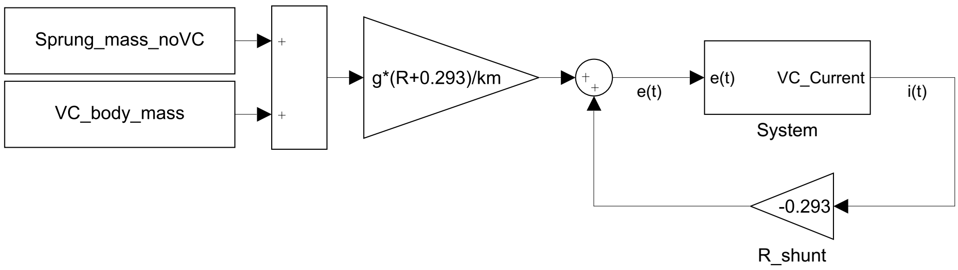

(a)

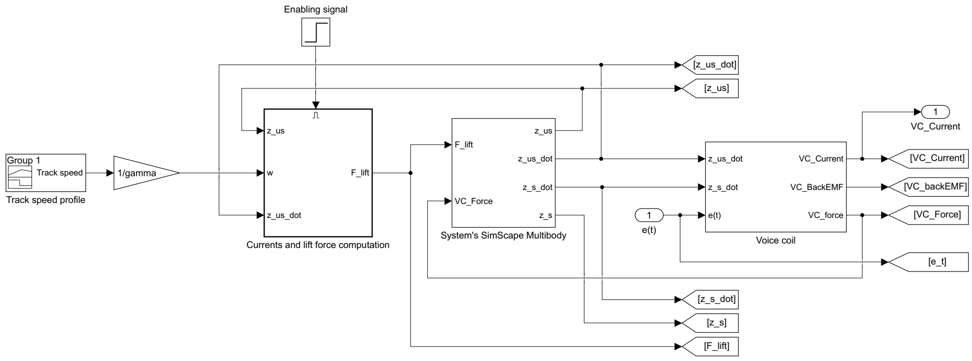

(b)

Figure 4.10: Passive damping control with current feedback and feedforward weight compensation, *Simulink* implementation.

Simulation results

To test the performance of the different control strategies, the system is simulated by providing a tangential velocity profile of the copper track similar to that in figure 4.6, imposing a steady state limit velocity of 19.69 m/s, which corresponds to 400 rpm. In addition, at time instant $t = 15s$, a disturbance corresponding to a 1 mm step in the copper track is introduced into the system, in order to observe the behavior of the control system in the presence of an instantaneous air gap change.

The first interesting observation concerns the position of the unsprung mass with respect to the copper track (i.e. the airgap) before and after the introduction of the disturbance component into the control system. A step of -1 mm amplitude is introduced on the airgap, and the system is expected to react accordingly. What is observed from the simulations is that due to the presence of the springs of stiffness k_{us} between the stator and the unsprung mass, the system does not reestablish the airgap condition prior to the introduction of the disturbance, but finds its equilibrium point with a smaller airgap. In contrast, setting the stiffness value k_{us} of the springs between the stator and unsprung mass to a very small value (1 Ns/m) does not allow the same behavior to be observed, but the airgap is restored to the condition prior to the introduction of the disturbance within the system.

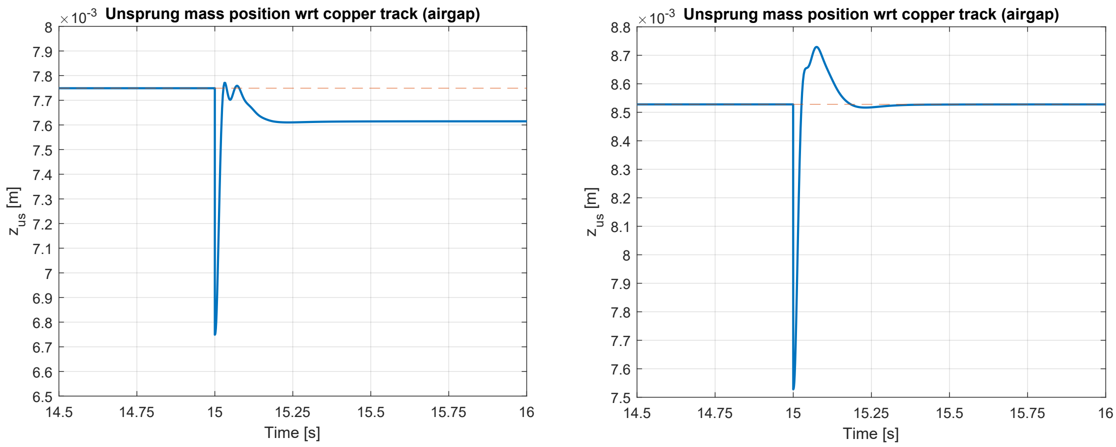

(a) $k_{us} = 8 \times 527\, Ns/m$. (b) $k_{us} = 1\, Ns/m$.

Figure 4.11: Unsprung mass position wrt copper track (the airgap) @ different k_{us} values.

Indeed, a step disturbance of 1 mm amplitude implies that the unsprung mass (and the whole system accordingly) reacts by varying its position relative to the stator. In turn, this implies that the springs will exert a greater resistance force opposing the displacement, thus causing a greater lift force needed to balance the system. Since the disturbance is introduced into the control system at a constant copper track tangential velocity, the only way to provide the lift force needed to balance the system lies in a smaller airgap value.

The position (with respect to a reference frame integral to the aluminum disk, at the base of the copper track) and velocity behavior of both sprung and unsprung masses are recorded, along with the characteristic quantities of the electrical domain of the secondary suspension. Moreover, the performance indices are reported in table 4.3 both for the unsprung mass and the sprung mass.

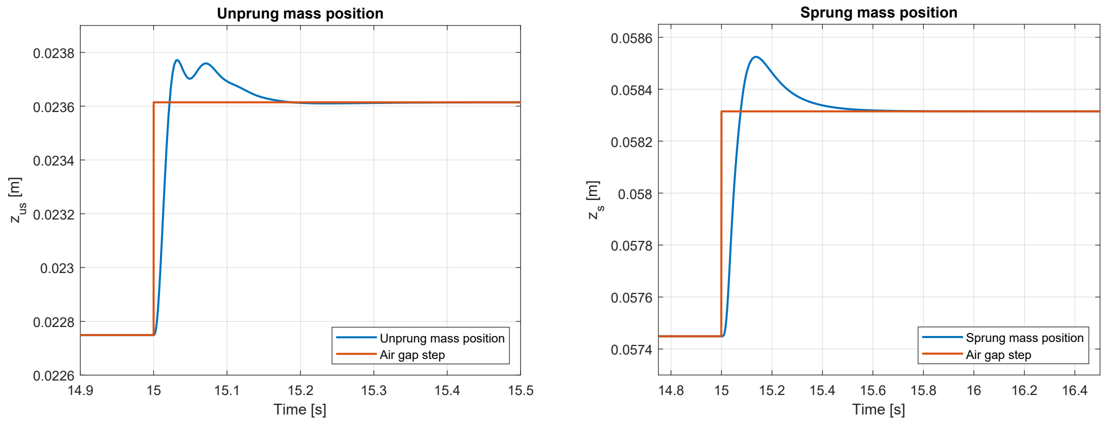

(a) Unsprung mass position. (b) Sprung mass position.

Figure 4.12: Unsprung and sprung mass position.

Performance index	**Unsprung mass m_{us}**	**Sprung mass m_s**
Percent overshoot	18.08%	24.25%
Peak time [s]	0.031	0.136
Settling time [s]	0.149	0.432

Table 4.3: Performance indeces .

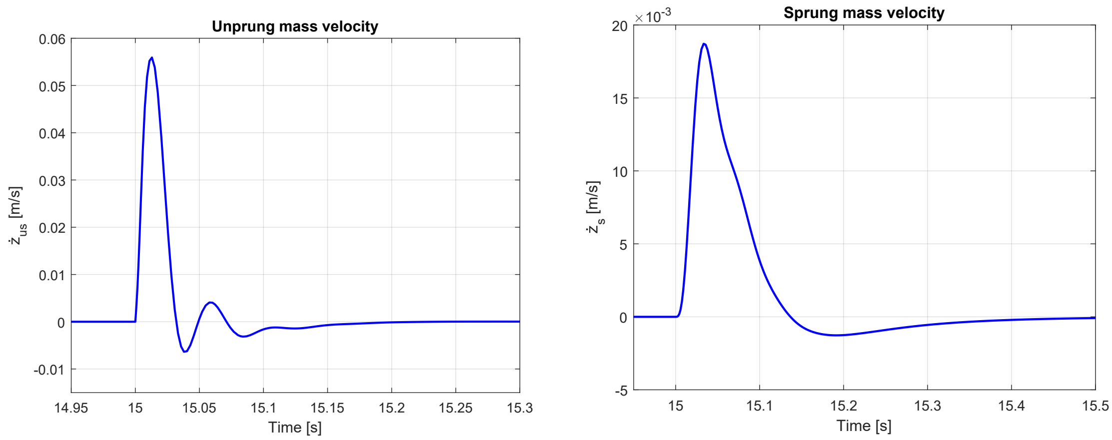

(a) Unsprung mass velocity. (b) Sprung mass velocity.

Figure 4.13: Unsprung and Sprung mass velocity.

The behaviors of the quantities related to the electrical domain of the VCA are shown in the graphs below, specifically the current flowing within the secondary suspension i(t) that is feedbacked to close the control system and the imposed voltage e(t) to drive the VCA.

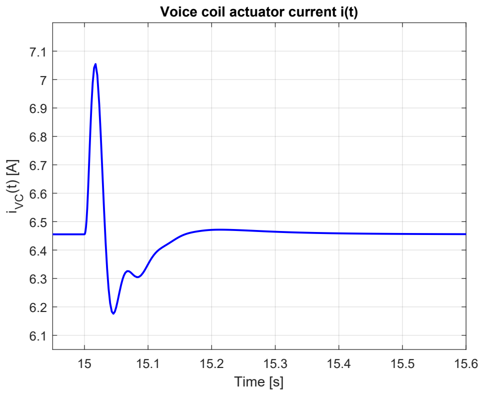

(a) Voice coil current i(t).

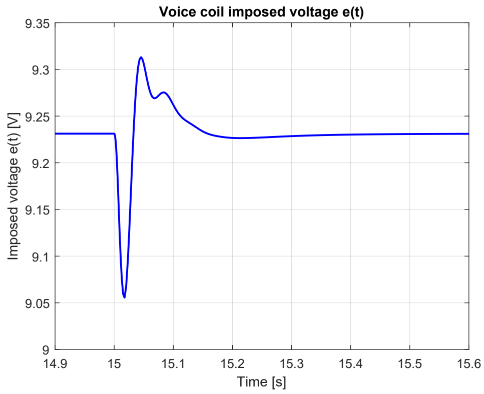

(b) Voice coil imposed voltage e(t).

Figure 4.14: Voice coil actuator electrical quantities behaviour.

The current never exceeds the maximum output current that the voice coil actuator can sustain given in table 4.1.

4.1.2 Open loop damping control with feedforward weight compensation

The following control strategy considers the VCA imposed voltage e(t) as the control input to the plant. The relative velocity between the sprung mass and the unsprung mass is feedbacked and it is multiplied by the optimal damping coefficient value c_{opt} in order to generate the optimal damping force reference. Together with the weight force reference for the sprung mass compensation, the total force reference is computed, which is later converted into the imposed voltage signal e(t) transmitted to the plant. This is possible by considering a static equation between the electrical quantities related to the voice coil and the force constant relation between the VCA current i(t) and the generated force F(t):

$$\begin{cases} e(t) = Ri(t) \\ F(t) = Kmi(t) \end{cases} \tag{4.8}$$

The scheme of the control system and its implementation in *Simulink* are shown in the figures below:

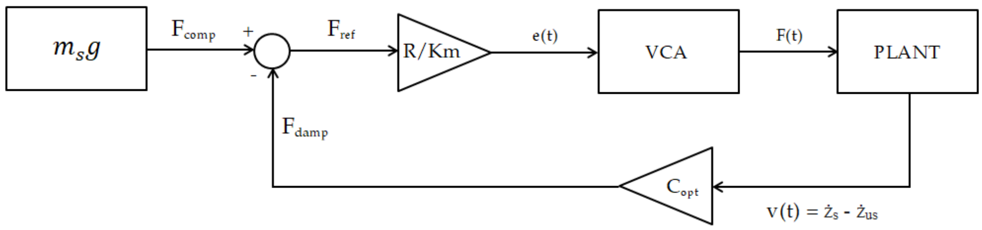

Figure 4.15: Open loop damping control with feedforward weight compensation, control system architecture.

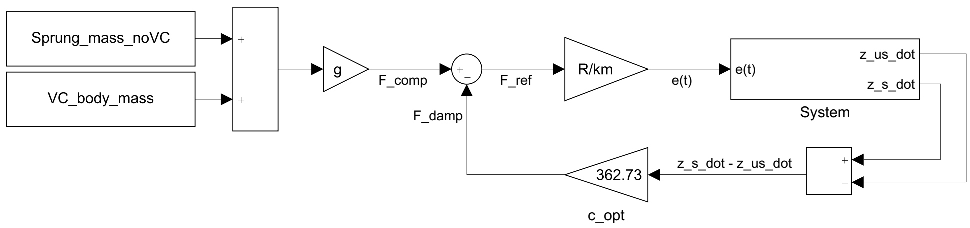

Figure 4.16: Open loop damping control with feedforward weight compensation, *Simulink* implementation.

Simulation results

The system is simulated by providing a tangential velocity profile of the copper track and a step disturbance in the air gap as in section 4.1.1. The position and velocity behavior of both sprung and unsprung masses are reported in the figures below, along with the performance indices computed for the current control strategy.

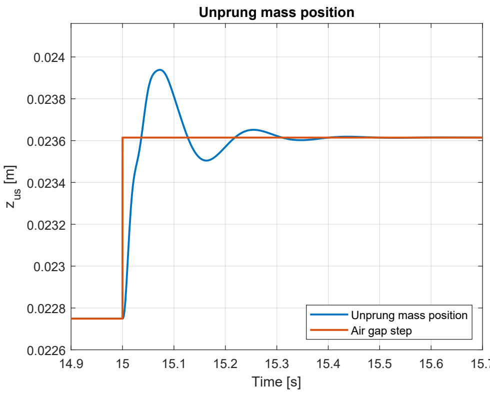

(a) Unsprung mass position.

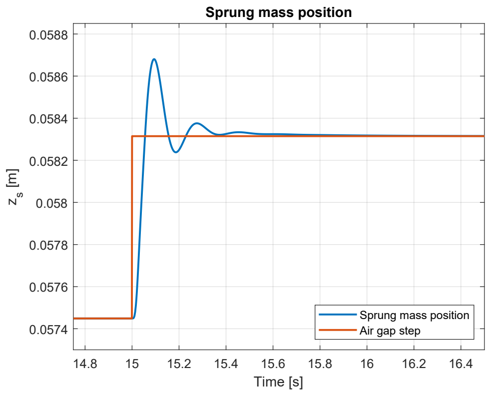

(b) Sprung mass position.

Figure 4.17: Unsprung and sprung mass position.

Performance index	**Unsprung mass m_{us}**	**Sprung mass m_s**
Percent overshoot	37.44%	42.27%
Peak time [s]	0.073	0.094
Settling time [s]	0.289	0.478

Table 4.4: Performance indeces.

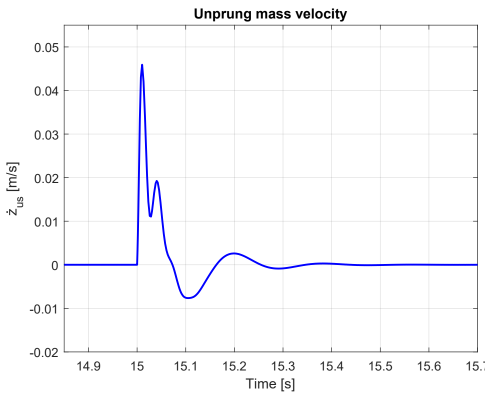

(a) Unsprung mass velocity.

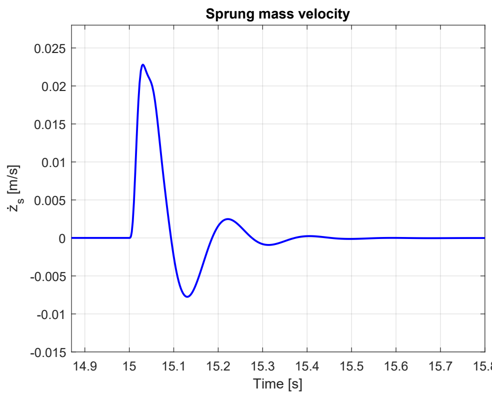

(b) Sprung mass velocity.

Figure 4.18: Unsprung and Sprung mass velocity.

In relation with the control strategy described in the previous section, larger oscillations can be observed in the position of the sprung mass and unsprung mass due to the implementation of an open-loop control that does not provide a more responsive controlled damping response. The behaviors of the current i(t) and imposed voltage e(t) related to the voice coil actuator are shown in the figures below.

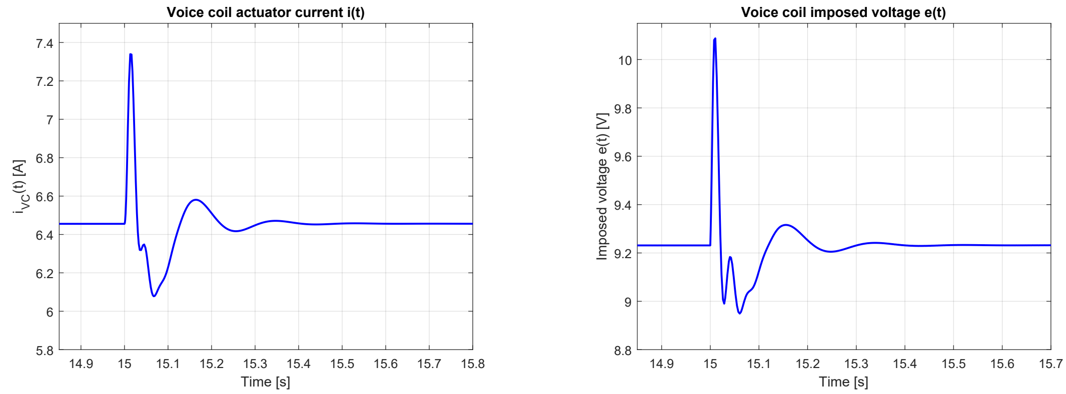

(a) Voice coil current i(t).

(b) Voice coil imposed voltage e(t).

Figure 4.19: Voice coil actuator electrical quantities behaviour.

Again, the current flowing within the VCA never exceeds the maximum value borne by the secondary suspension.

4.1.3 Closed loop current control with PI controller and feedforward weight compensation

In the control strategy described in the following section, the VCA is again driven by imposing the voltage e(t) and using it as the control input to the system. As in the previous case, the force references remain the same, namely the component F_{comp} needed to compensate for the weight of the sprung mass and the component F_{damp} needed to introduce the optimal damping within the control system. The latter force component is computed through the relative velocity v(t) between the sprung mass and the unsprung mass and the optimal damping coefficient c_{opt}. In this case, differently from the control strategy in the previous section, the current reference i_{ref} that must flow within the secondary suspension to ensure the double contribution of damping and sprung mass compensation is computed from the force reference F_{ref} by means of the equation 4.1. A current loop with a PI controller is implemented to ensure that the reference current is maintained within the VCA. The controller is also responsible for converting the error signal on the current $i_{err(t)}$ into a voltage signal e(t) to be transmitted directly to the system.

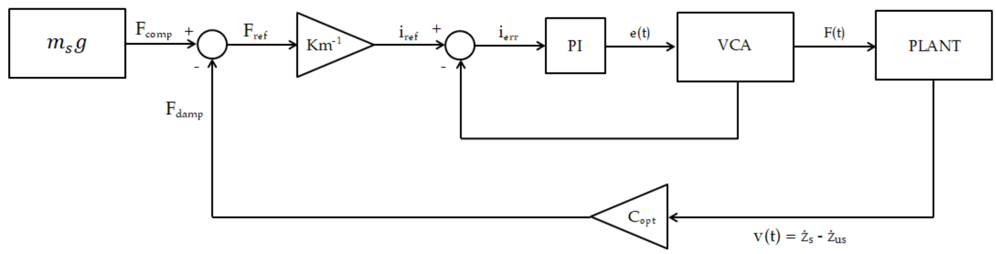

Figure 4.20: Closed loop current control with PI controller and feedforward weight compensation, control system architecture.

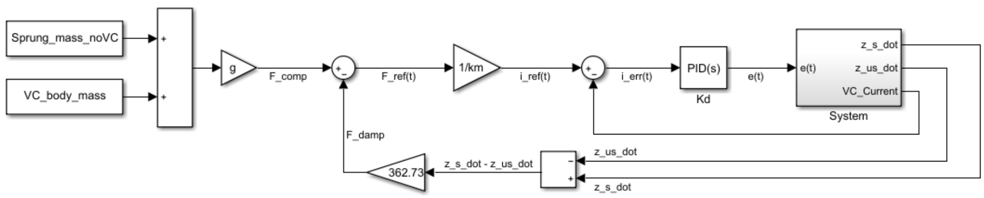

Figure 4.21: Closed loop current control with PI controller and feedforward weight compensation, *Simulink* implementation.

The PI controller is based on the following transfer function that links the output (control input to the plant, $e(t)$) and the input (error on the current, $i_{err(t)}$):

$$e(t) = \left[P \left(1 + I\frac{1}{s} + D\frac{N}{1+N\frac{1}{s}} \right) \right] i_{err(t)} \tag{4.9}$$

where P,I and D are the PID controller's proportional, integral and derivative coefficient, s the complex number proper to the Laplace transform and N the filter coefficient.

A PI-type controller is chosen because the derivative term can introduce instability and large oscillations when dealing with noisy systems and signals. As for the proportional P and integrative I terms, two different sets of values are simulated and are reported below in table 4.5.

Sets of values	**P**	**I**
1^{st} set	69.74	128.83
2^{nd} set	0.7	96.62

Table 4.5: P,I coefficient values.

Experimental results

The system is again simulated by providing a tangential velocity profile of the copper track and a step disturbance in the air gap as in section 4.1.1. The position behaviour of the sprung mass for both the 1^{st} and the 2^{nd} sets of values for the P, I coefficient are reported in the figures below, toghether with the behaviour of the imposed voltage e(t) that drives the VCA. The trends refer to the entire simulation duration and include both the sprung mass compensation transient and the introduction of the step disturbance into the air gap profile.

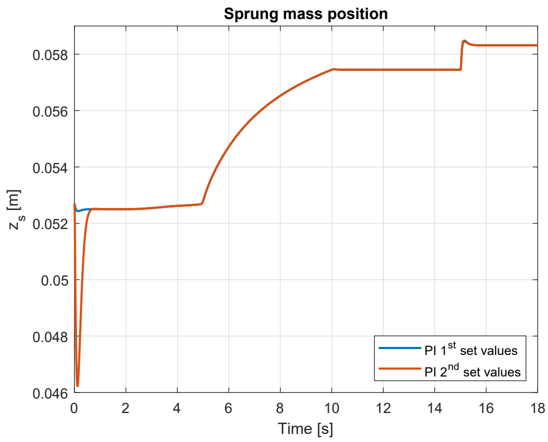

Figure 4.22: Sprung mass position.

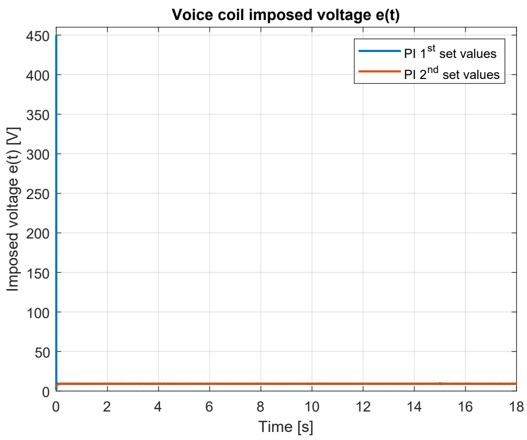

(a) Voice coil Imposed voltage e(t).

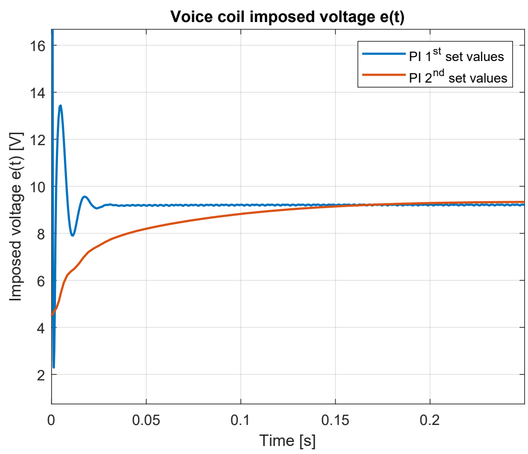

(b) Voice coil imposed voltage e(t) - Zoom.

Figure 4.23: Voice coil imposed voltage e(t).

By choosing the PI coefficients belonging to the first set of values it is possible to obtain a much more reactive response to the sprung mass compensation, which however leads to a consequent substantial increase in terms of driving voltage of the voice coil actuator with $e_{max}(t) = 450.22\,V$. Instead, with the PI coefficients of the second set of values it is possible to contain the voice coil imposed voltage e(t) at the expense of a lower reactivity of the control system. The performance, in terms of reaction to a step disturbance on the air gap, is very similar for both sets of values of the PI controller and is reported in the graphs below for both sprung and unsprung masses.

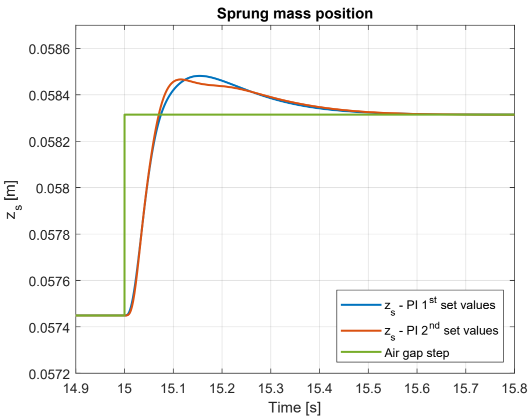

(a) Unsprung mass position.

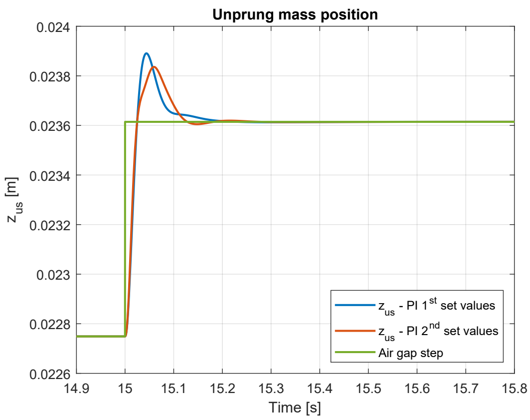

(b) Sprung mass position.

Figure 4.24: Unsprung and sprung mass position.

Set of values	Performance index	m_{us}	m_s
PI 1^{st} set of values	Percent overshoot	31.92%	19.31%
	Peak time [s]	0.044	0.154
	Settling time [s]	0.149	0.442
PI 2^{nd} set of values	Percent overshoot	25.61%	17.50%
	Peak time [s]	0.060	0.114
	Settling time [s]	0.117	0.461

Table 4.6: Performance indices.

The behaviors of the velocities of both unsprung and sprung mass along with the current i(t) and imposed voltage e(t) related to the voice coil actuator for both PI coefficient's sets of values are shown in the figures below.

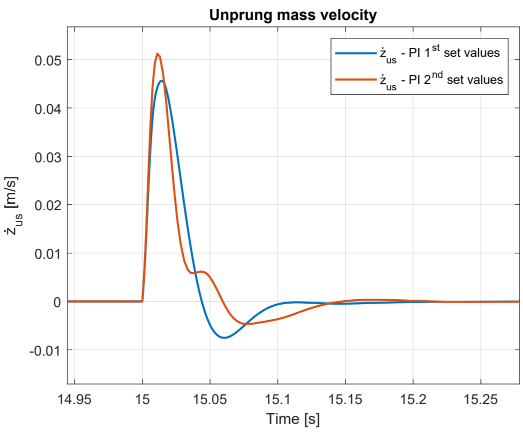

(a) Unsprung mass velocity.

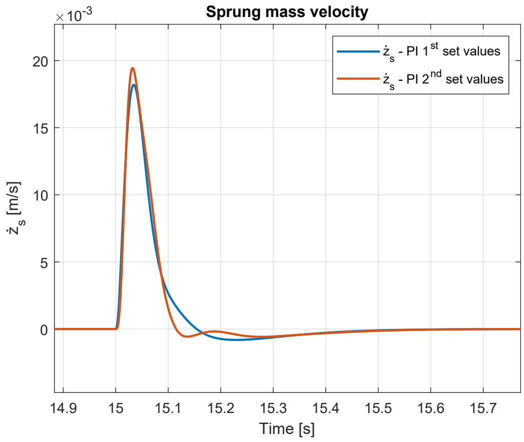

(b) Sprung mass velocity.

Figure 4.25: Unsprung and Sprung mass velocity.

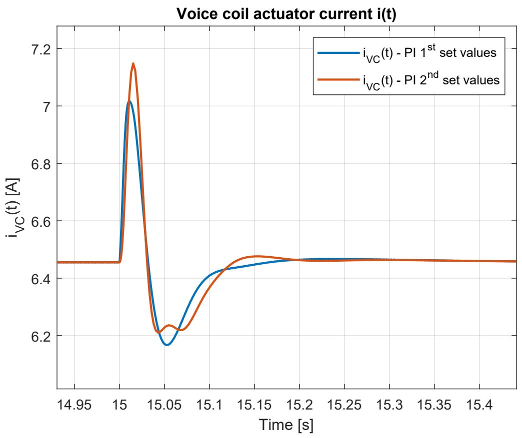

(a) Voice coil current i(t).

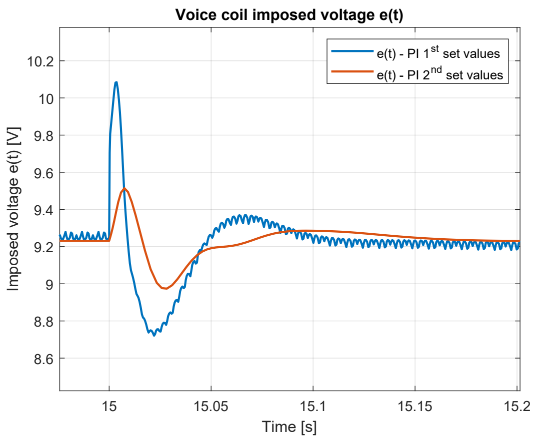

(b) Voice coil imposed voltage e(t).

Figure 4.26: Voice coil actuator electrical quantities behaviour.

It is possible to observe from figure 4.26b an oscillation in the imposed voltage e(t) of the VCA regarding the 1^{st} set of PI coefficient. Moreover, the currents never exceed the limit value borne by the secondary suspension.

Chapter 5

Velocity estimation

In the previous chapter, which deals with the different control strategies for the stabilization of the dynamic stage, it is clear that an accurate estimation of the relative velocity between the masses of the system is fundamental to ensure the implementation of the optimal damping. The absence of sensors on the test bench, which allow a direct measurement of the quantities necessary for the control systems, induce the introduction of sensorless algorithms for the estimation of the latter. This chapter discusses two different sensorless algorithms for the estimation of the relative velocity between sprung mass and unsprung mass and multibody simulation to test their performance. Moreover, in the second part of this chapter, the control strategy that has the best performance is tested considering to implement a relative speed estimator and no longer the ideal signal from the multibody system.

5.1 VCA Simscape Multibody's modelling

For the simulation and testing of the performance of the different speed estimation algorithms it is chosen to implement a stand-alone multibody model of the voice coil actuator, considering as the only mobile mass of the system the VCA mover. It is possible to represent the mechanical model through the following equation:

$$m\ddot{x} + c\dot{x} + mg = Kmi(t) \tag{5.1}$$

where m is the voice coil mover mass, c is the proper damping coefficient of the VCA, Km is the force constant and $i(t)$ is the current that flows in the secondary suspension. For what concern the proper damping of the voice coil actuator, the characterization procedure is reported in the thesis of the colleague Arianna Conchin Gubernati and leads to the value of the damping coefficient $c = 207Ns/m$.

The multibody model developed in *Simscape Multibody* and a 3D representation of the system are shown in the figures below.

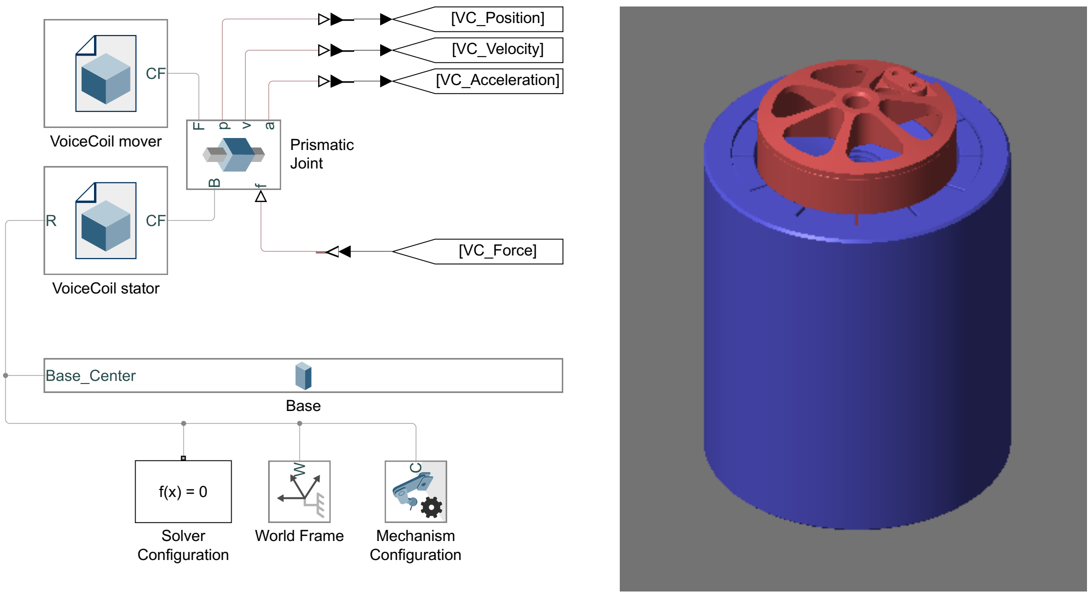

(a) *Simscape Multibody* model. (b) 3D graphical representation.

Figure 5.1: Mechanical domain's *Simscape Multibody* model of the VCA.

The mechanical domain is closely related to the electric domain of the voice coil actuator, which is also modeled in Simulink considering a simplified RL model as described in section 4.0.1.

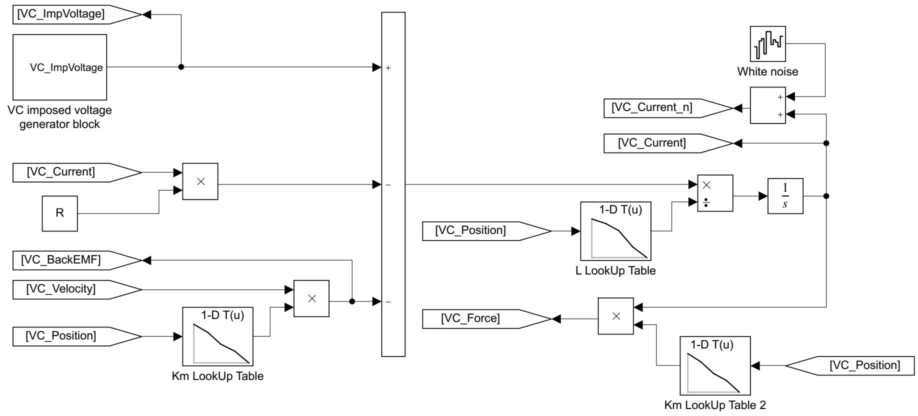

Figure 5.2: Electrical domain's *Simscape Multibody* model of the VCA.

Within the RL model of the electric domain of the voice coil actuator changes are introduced on the inductance L and on the force constant Km depending on the position of the mover with respect to the stator of the VCA with the aim of simulating a behavior of the model the most similar to the real system. This is done by means of two Look Up Tables blocks in *Simulink*, the behaviors of L and Km as a function of the VCA mover position are reported in figures 5.3a and 5.3b. In addition, a white noise is introduced on the measurement of the current flowing within the secondary suspension, which is then used in the estimation of the velocity.

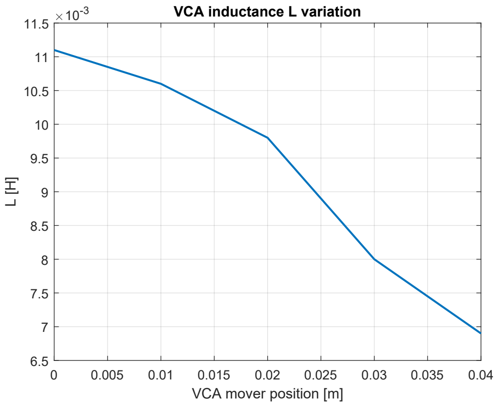

(a) L variation.

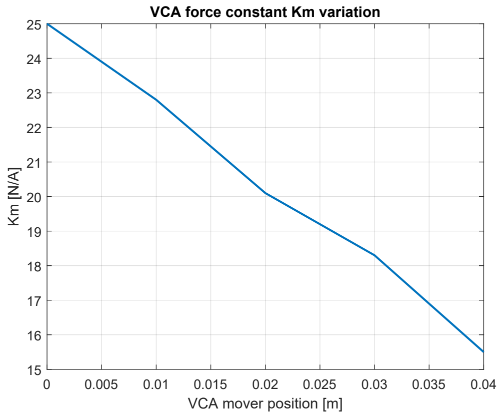

(b) Km variation.

Figure 5.3: VCA inductance L and force constant Km variations as a function of the mover position.

The system is driven by means of the imposed voltage e(t) to the RL circuit of the voice coil actuator with a chirp signal of variable frequency between 1 and 20 Hz with constant amplitude, and an offset corresponding to the constant voltage value necessary to compensate for the weight force of the mover. In addition, there is a 2s initial phase in which a higher voltage than the value necessary to compensate the weight force of the mover is provided, so that the mover can rise and avoid bumps against the stator during the oscillation phase. The behavior of the imposed voltage e(t) as a function of time is shown in the figure below. The performance of the different velocity estimators is compared by generating the gain and phase bode diagrams between the actual velocity signal from the multibody system and the estimated velocity signal and measuring the offset between the two.

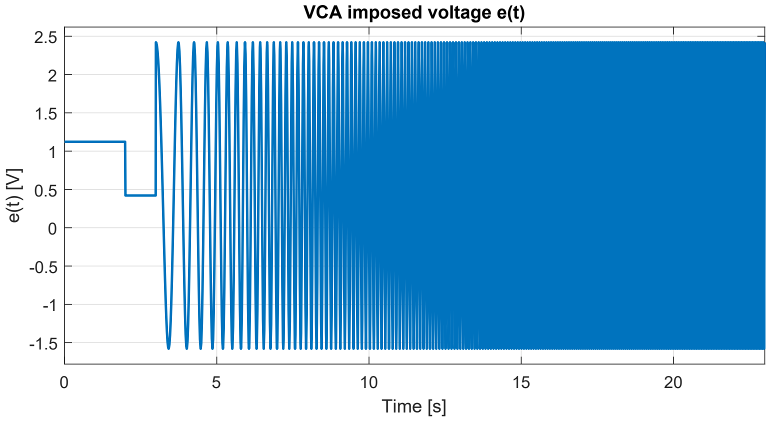

Figure 5.4: VCA imposed voltage e(t).

5.2 RL circuit velocity estimator

The characteristic equation that models the electric domain of the voice coil actuator via an RL circuit can be used as a velocity estimator, as it is possible to derive the value of the latter from the voltage term linked to the counter electromotive force. From equation 4.3 it is possible to derive:

$$v(t) = \frac{1}{Km}\left(e(t) - Ri(t) - L\frac{di(t)}{dt}\right) \quad (5.2)$$

where $v(t)$ is the relative velocity between the stator and the mover of the VCA. The figure below shows the model of the velocity estimator based on the RL circuit, which implements equation 5.2.

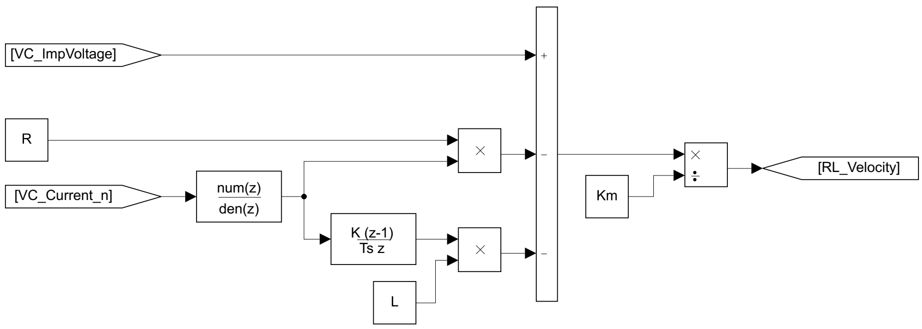

Figure 5.5: RL circuit velocity estimator, *Simulink* model.

Unlike the RL circuit that models the electrical domain of the VCA, for which variations on L and Km are generated depending on the position of the mover, from the point of view of the velocity estimator it is not possible to know the real behavior of the inductance L and the force constant Km. For this reason, constant estimated values for these quantities shall be used and the estimator performance shall be evaluated. In addition to this, it is crucial to use a low pass filter to filter the measured current flowing within the secondary suspension, because it must be derived to calculate the voltage drop on the inductance L and to obtain a less noisy velocity estimate. The implemented filter is a second order Butterworth discrete filter with cut off frequency at 200 Hz.

Experimental results

Below are reported the behaviors of the real velocity derived from the multibody model of the VCA and the behaviors of the velocity estimated through the RL circuit.

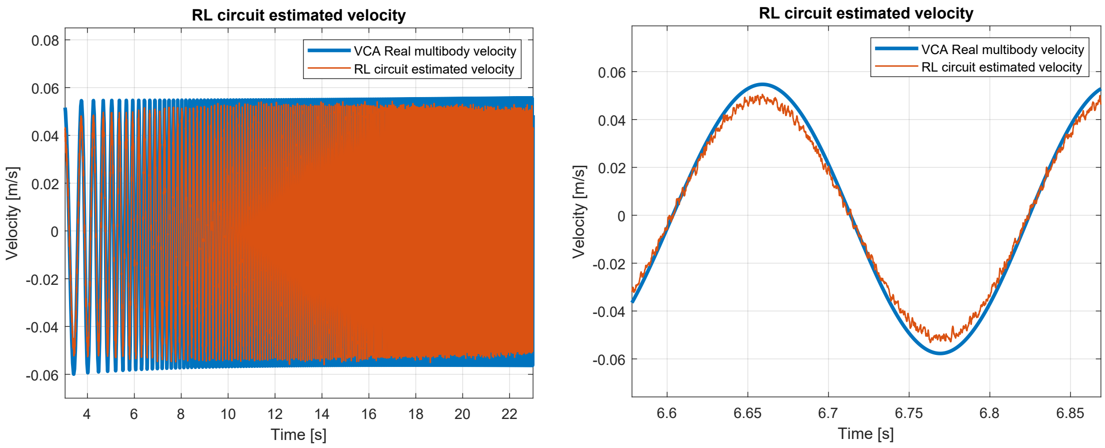

(a) Velocities behaviors.

(b) Velocities behaviors - zoom.

Figure 5.6: Real VCA multibody velocity and RL circuit estimated velocity.

To quantify the accuracy and performance of the estimator it is necessary to generate the bode diagram relative to the gain in amplitude between the real and the estimated velocities and relative to the phase shift between the two signals. The gain in amplitude is a dimensionless number, while the phase shift is reported in degrees.
It is possible to observe in figure 5.7 that increasing the oscillation frequency of the system the phase shift increases until a maximum of 3.5 deg at 20 Hz. This is due to the fact that a low pass filter has been introduced on the measured current to allow the calculation of the derivative and the voltage drop on the inductor L, and it involves a phase shift that increases with the frequency.

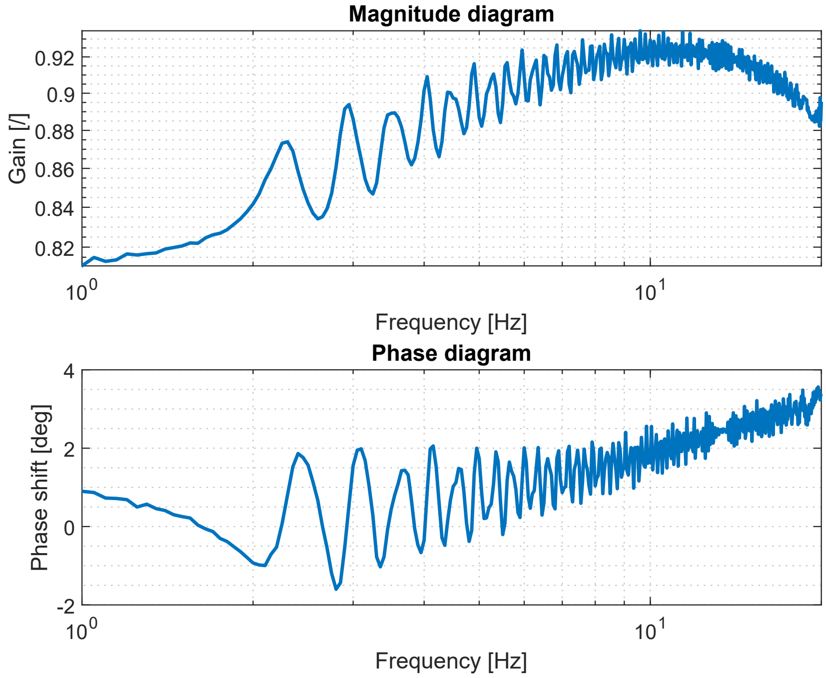

Figure 5.7: RL circuit velocity estimator, Bode diagram.

With regard to the magnitude bode diagram, a non-monotonous behavior of the gain between the two velocity signals can be observed. As described above, within the voice coil actuator model there are variations on inductance parameters L and force constant Km, resulting in a decrease in these quantities as the position of the mover relative to the secondary suspension stator increases. In the calculation of the constant voltage value for the compensation of the weight force of the mover a constant value of Km is used, as it is assumed not to know the extent of the variation on this parameter. This means that, after the initial lifting phase of the mover, the constant imposed voltage to compensate for the weight force of the latter is not sufficient to keep it in a constant raised position, but a descent is observed. If the mover is located in a position that implies a minor surface of the coil out from the magnetic field of the permanent magnets, the inductance L and force constant Km values will be closer to those used within the speed estimator model RL and the estimation will be more accurate. This is why it is possible to observe an increase in the gain between the two signals and a greater accuracy of the estimation. The decrease that can be observed at high frequencies is due to the variations on the L and Km parameters of the model and how they have been set and interact with each other.

5.3 Kalman filter velocity estimator

5.3.1 Theoretical background

The Kalman Filter is one of the most important and common estimation algorithms. Its objective is to produce an estimate of the true state of the system that cannot be directly observed by combining models of the system and noisy measurements of certain parameters or linear functions of parameters. The Kalman filter model is based on the assumption that the state of any system at a time k evolve from the prior state at time $k-1$ in accordance to the following equation:

$$x_k = F_k x_{k-1} + G_k u_k + w_k \tag{5.3}$$

where x_k and x_{k-1} are the state vectors respectively at time k and $k-1$, F_k is the state matrix which maps the influence of each state parameter at time $k-1$ on the system state at time t, u_k is the input matrix that contains any inputs to the system, G_k is the input matrix which applies the effect of each input on the state vector at time k, and w_k is the process uncertainty vector containing the process noise terms for each state variable. It is assumed that the process uncertainty has zero mean and covariance denoted by matrix Q_k.
Measurements on the system can be taken into account considering the following equation:

$$Z_k = H_k x_k + v_k \tag{5.4}$$

where z_k is the measurements vector, H_k is the measurements matrix that applies the effect of the state vector parameters into the measurement domain and v_k is the measurement uncertainty which is assumed to have zero mean and covariance denoted by matrix R_k.
The estimates of the parameters of the state vector are derived from the combination of different gaussian probability density functions (pdfs) associated with the predictions based on the system's model and with the measurements performed on the system. Therefore, the Kalman filter estimation algorithm is composed by two different stages: a prediction stage and a measurement update stage. The prediction stage is characterized by equations:

$$\begin{cases} \bar{x}_k = F_k x_{k-1} + G_k u_k \\ \bar{P}_k = F_k P_{k-1} F_k^T + Q_k \end{cases} \tag{5.5}$$

The first equation is responsible for the calculation of the state estimation of the system through the analytical model of the latter, the second equation instead deals with the calculation of the covariance matrix $\bar{P}_k$. The measurement update stage equation are:

$$\begin{cases} K_k = \bar{P}_k H_k^T \left(H_k \bar{P}_k H_k^T + R_k \right)^{-1} \\ x_k = \bar{x}_k + K_k \left(z_k - H_k \bar{x}_k \right) \\ P_k = \left(I - K_k H_k \right) \bar{P}_k \end{cases} \tag{5.6}$$

and allow the calculation of the Kalman filter gain K_k at time k in order to calculate and update the system state prediction x_k and the covariance matrix P_k. To compute the correction of x_k, the measurement vector z_k is required.

5.3.2 Kalman filter implementation

In the case of this treatment, through the use of an estimation algorithm based on the Kalman filter it is possible to merge the information coming from the mechanical model and the electrical model of the system. The system under consideration can be described from a mechanical point of view by considering a mass, representing the mass of the VCA mover, and a damper that allow the introduction of the proper damping of the secondary suspension as reported below.

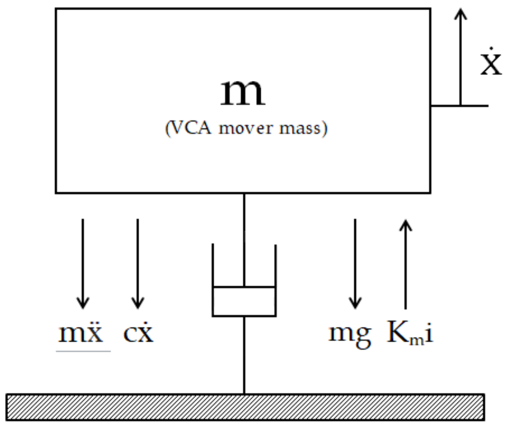

$$\begin{aligned} m\ddot{x} + c\dot{x} + mg &= K_m i \\ \ddot{x} &= -\frac{c}{m}\dot{x} + \frac{K_m}{m} i - g \end{aligned} \tag{5.7}$$

The equations representing the electrical domain of the secondary suspension are given below for reasons of clarity of exposure:

$$\begin{aligned} e(t) &= Ri(t) + L\frac{di(t)}{dt} + v_{backEMF}(t) \\ e(t) &= Ri(t) + L\frac{di(t)}{dt} + K_m \dot{x} \\ \frac{di(t)}{dt} &= -\frac{Km}{L}\dot{x} - \frac{R}{L} i(t) + \frac{1}{L} e(t) \end{aligned} \tag{5.8}$$

Through a state space representation of the system equations it is possible to write the equations of the Kalman filter:

$$\begin{aligned} \begin{bmatrix} \ddot{x} \\ \dot{i} \end{bmatrix} &= \begin{bmatrix} -\frac{c}{m} & \frac{Km}{m} \\ -\frac{Km}{L} & -\frac{R}{L} \end{bmatrix} \begin{bmatrix} \dot{x} \\ i \end{bmatrix} + \begin{bmatrix} -1 & 0 \\ 0 & \frac{1}{L} \end{bmatrix} \begin{bmatrix} g \\ e(t) \end{bmatrix} + G(t)w(t) \\ i &= \begin{bmatrix} 0 & 1 \end{bmatrix} \begin{bmatrix} \dot{x} \\ i \end{bmatrix} + \begin{bmatrix} 0 & 0 \end{bmatrix} \begin{bmatrix} g \\ e(t) \end{bmatrix} + H(t)w(t) + v(t) \end{aligned} \tag{5.9}$$

The first is the state equation of the system while the second represents the measurements equation. $G(t)$ represents the mapping between process noise terms and state variables and its default value is the identity matrix I, while $H(t)$ represent the mapping between process noise terms and measured variables and its default value is 0. As can be seen from the equations, it is assumed that the only measured signal is the current flowing within the VCA.
In *Simulink*, the Kalman Filter block already implements the equations of the state estimation algorithm and it only necessitate of the information on the characteristic matrices of the state space representation, as well as the covariances matrices Q_k and R_k.

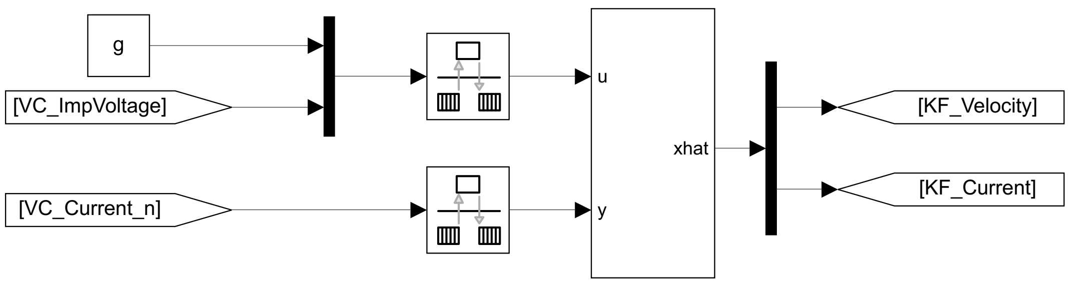

Figure 5.8: Kalman Filter implementation in *Simulink*.

To set the value of the covariance matrix R consider the white noise imposed on the current i(t) measured within the secondary suspension. It is shown in the figure below:

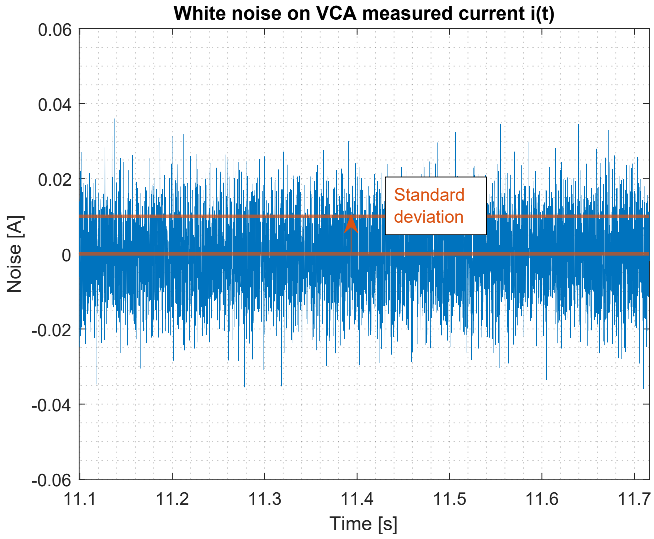

Figure 5.9: Noise on measured current i(t).

The standard deviation σ of the signal is equal to 0.01, and for this reason the covariance matrix R is set to:

$$R = \sigma^2 = (0.01)^2 = 1 \cdot 10^{-4} \tag{5.10}$$

The values of the covariance matrix Q instead are set by a tuning procedure, and at the end it results:

$$Q = \begin{bmatrix} 0.005 & 0 \\ 0 & 0.1 \end{bmatrix} \tag{5.11}$$

Moreover, the matrix $G(t)$ and $H(t)$ are left as default values.

Experimental results

The Kalman filter allows the estimation of the current within the VCA and the relative speed of the mover with respect to the suspension stator, which are the states of the system under study. Since the current is also measured directly, the estimate of the latter will be almost perfect. The behavior of the current i(t) measured and estimated by the Kalman filter, together with the behavior of the real velocity from the multibody model and the estimated velocity are shown below.

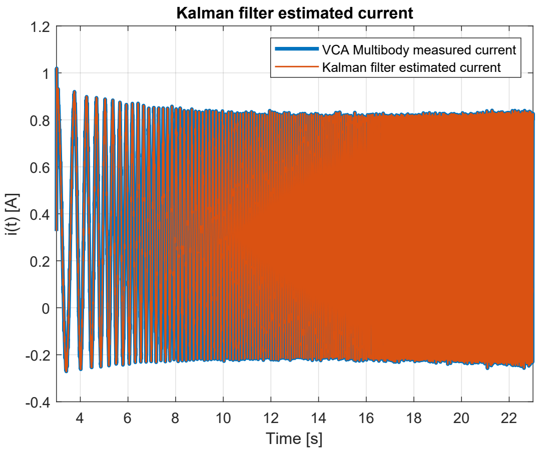

(a) Current behaviors.

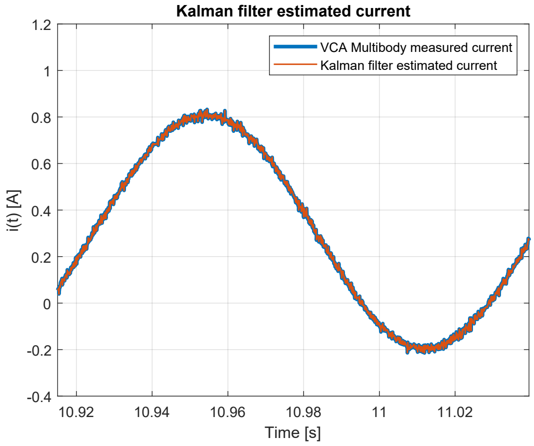

(b) Current behaviors - zoom.

Figure 5.10: VCA multibody measured current and Kalman filter estimated current.

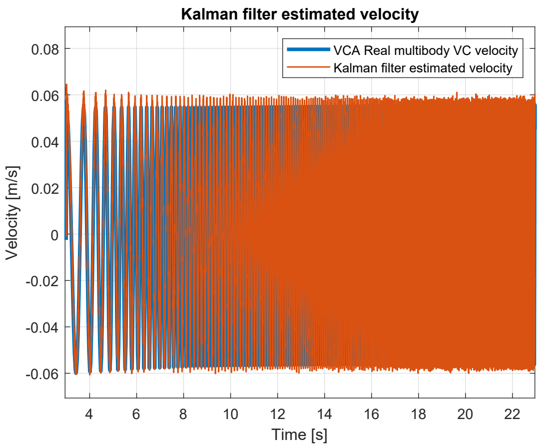

(a) Velocities behaviors.

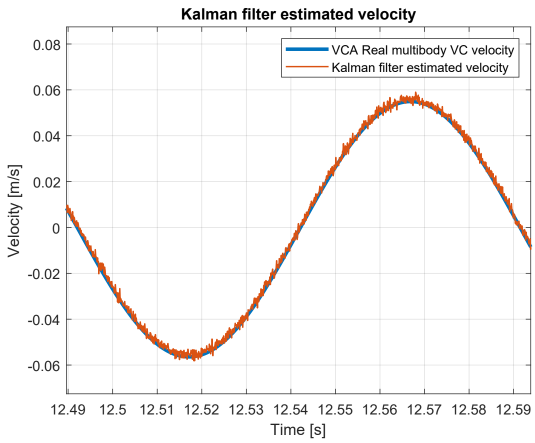

(b) Velocities behaviors - zoom.

Figure 5.11: Real VCA multibody velocity and Kalman filter estimated velocity.

In addition, it is reported below the bode diagram characterized by the behaviors of the gain and the phase shift between the real velocity signals of the multibody model and the velocity estimated by the Kalman filer. The gain is always constant and unitary to the variation of the oscillation frequency, while the phase shift for higher frequencies tends to a value close to 0 degrees.

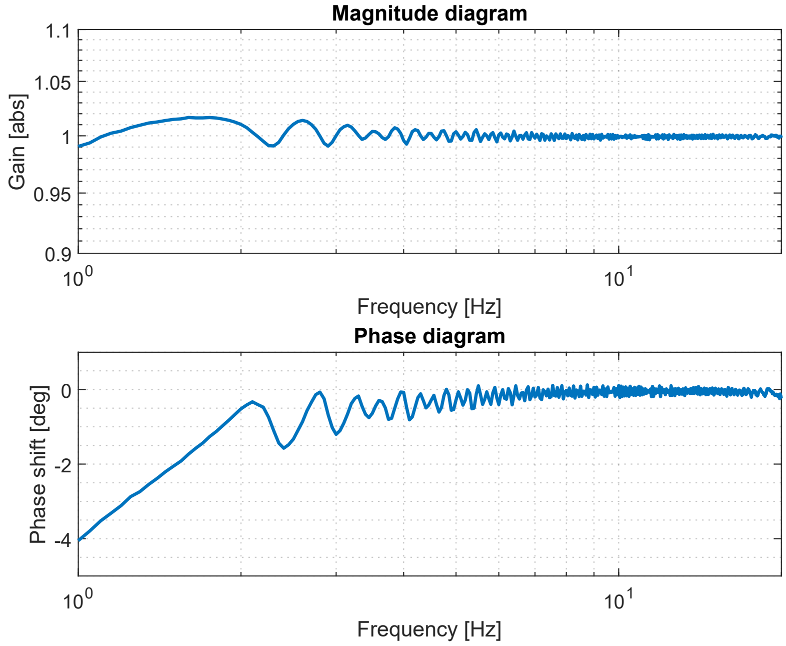

Figure 5.12: Kalman filter estimator, Bode diagram.

In addition, a slight offset is observed in the velocity estimation due to the presence of variations on inductance L and force constant Km parameters.

Chapter 6

Conclusions and further studies

In recent years, the urgent need to limit the use of fossil fuels and the emission of gases that contribute to the increase in the greenhouse effect is becoming an increasingly debated issue and the urgency to take action in this direction is unequivocal. Transport is certainly one of those areas where action is needed through the introduction of new, sustainable technologies. In this context, Hyperloop represents the possibility to implement a new transport system based on the magnetic levitation principle allowing to drastically reduce air Pollution and fitting optimally in this framework. The levitation subsystem, which exploits the principle of passive electrodynamic levitation and which is the key factor on which the transport system is based, involves an intrinsically unstable behaviour, that has been studied and rigorously assessed by Galluzzi et al. The analytical modeling of the interaction between the electromagnetic domain, with the description of the distribution of eddy currents, and the mechanical domain that describes the vertical dynamics of the system has made possible the identification of the instability that arises from the interaction between the two different domains and the characterization of the damping necessary to ensure stabilization.
The second chapter of this thesis opens with the characterization of the test bench on which the experimental tests will be conducted. An accurate characterization of the various elements that compose the system, as well as the measurement systems, is necessary so that it is possible to evaluate possible non-idealities to be taken into account and possibly correct them. Thanks to this work, it is possible to guarantee the accuracy of the experimental results obtained during the conduction of the experimental tests of quasi-static nature presented in the thesis. The obtained results made it possible to identify the parameters of the analytical model that describes the interaction between the electrodynamic domain and the mechanical domain, and the consequent identification of the instability and the damping necessary to stabilize the system. In this context, the results are very satisfactory and allow, through the RL lumped parameter model, to describe the

different forces trends, involved during the operation of the system, with sufficient accuracy. The multibody modelling of the entire levitation system allowed to implement different control strategies in simulation, and to test their performance. The need to acquire the velocity signals of the masses, fundamental for the implementation of the control techniques, has opened the need to introduce, from the simulation point of view, algorithms for the estimation of these quantities. Two different velocity estimation techniques have been introduced and the performance has been tested, yielding satisfactory results.
The testing of the velocity estimation algorithms on the real system and the implementation on the test bench of the different control techniques is left for future studies.

Bibliography

[1] Kemal ARMAĞAN. The fifth mode of transportation: Hyperloop. *Journal of Innovative Transportation*, 1(1):1105, 2020.

[2] Josh Giegel. Future travel: Hyperloop could be the missing link in making mobility greener. URL: https://www.euronews.com/next/2021/07/01/future-travel-hyperloop-could-be-the-missing-link-in-making-mobility-greener.

[3] Robert Goddard. Vacuum tube transportation system. U.S. Patent 2 511 979, June 20 1950.

[4] Hyung-Woo Lee, Ki-Chan Kim, and Ju Lee. Review of maglev train technologies. *IEEE transactions on magnetics*, 42(7), 2006.

[5] Elon Musk. Hyperloop alpha, 2013. URL: https://www.tesla.com/sites/default/files/blog_images/hyperloop-alpha.pdf.

[6] Richard F Post and Dmitri Ryutov. The inductrack concept: A new approach to magnetic levitation. Technical report, Lawrence Livermore National Lab.(LLNL), Livermore, CA (United States), 1996.

[7] Andrea Tonoli. Dynamic characteristics of eddy current dampers and couplers. *Journal of Sound and Vibration*, 301(3-5):576–591, 2007.

[8] Andrea Tonoli, Nicola Amati, Fabrizio Impinna, and Joaquim Girardello Detoni. A solution for the stabilization of electrodynamic bearings: Modeling and experimental validation. *Journal of vibration and acoustics*, 133(2), 2011.

[9] Fabrizio Impinna, Joaquim Girardello Detoni, Nicola Amati, and Andrea Tonoli. Passive magnetic levitation of rotors on axial electrodynamic bearings. *IEEE Transactions on Magnetics*, 49(1):599–608, 2012.

[10] JG Detoni, F Impinna, A Tonoli, and N Amati. Unified modelling of passive homopolar and heteropolar electrodynamic bearings. *Journal of sound and vibration*, 331(19):4219–4232, 2012.

[11] Alexei V Filatov and Eric H Maslen. Passive magnetic bearing for flywheel energy storage systems. *IEEE Transactions on Magnetics*, 37(6):3913–3924, 2001.

[12] Torbjörn A Lembke. *Design and analysis of a novel low loss homopolar electrodynamic bearing*. PhD thesis, KTH, 2005.

[13] T. A. Lembke. Review of electrodynamic bearings. ISMB14, Aug. 11–14. 14th International Symposium on Magnetic Bearings.

[14] T. A. Lembke. Electrodynamic actuator, 2008. Patent application WO2010064978.

[15] T. A. Lembke. 1-dof bearing arrangement with passive radial bearings and highly efficient integrated electrodynamic dampers, edd. ISMB13, Aug. 6–9 2012. 13th International Symposium on Magnetic Bearings, Arlington, VA.

[16] Joachim Van Verdeghem, Virginie Kluyskens, and Bruno Dehez. Five degrees of freedom linear state-space representation of electrodynamic thrust bearings. *Journal of Sound and Vibration*, 405:48–67, 2017.

[17] Joachim Van Verdeghem, Virginie Kluyskens, and Bruno Dehez. Stability and performance analysis of electrodynamic thrust bearings. In *Actuators*, volume 8, page 11. Multidisciplinary Digital Publishing Institute, 2019.

[18] Richard F Post. Inductrack demonstration model. Technical report, Lawrence Livermore National Lab.(LLNL), Livermore, CA (United States), 1998.

[19] Richard F Post and Dmitri D Ryutov. The inductrack: a simpler approach to magnetic levitation. *IEEE Transactions on applied superconductivity*, 10(1):901–904, 2000.

[20] Ove F Storset and Brad Paden. Infinite dimensional models for perforated track electrodynamic magnetic levitation. In *Proceedings of the 41st IEEE Conference on Decision and Control, 2002.*, volume 1, pages 842–847. IEEE, 2002.

[21] Sam Gurol and Bob Baldi. Overview of the general atomics urban maglev technology development program. In *ASME/IEEE Joint Rail Conference*, volume 41634, pages 187–191, 2004.

[22] Husam Gurol, Robert Baldi, Phillip Jeter, In-Kun Kim, Daryl Bever, and General Atomics. General atomics low speed maglev technology development program (supplemental# 3). Technical report, United States. Federal Transit Administration. Office of Technology, 2005.

[23] Hitoshi Tsunashima and Masato Abe. Static and dynamic performance of permanent magnet suspension for maglev transport vehicle. *Vehicle System Dynamics*, 29(2):83–111, 1998.

[24] Roshan Pradhan and Aditya Katyayan. Vehicle dynamics of permanent-magnet levitation based hyperloop capsules. In *Dynamic Systems and Control Conference*, volume 51906, page V002T22A004. American Society of Mechanical Engineers, 2018.

[25] Mohammed M Khan. Development of ryerson's hyperloop pod systems using a modular approach. In *International Conference on Aerospace System Science and Engineering*, pages 209–218. Springer, 2019.

[26] MMJ Opgenoord, C Merian, J Mayo, P Kirschen, C O'Rourke, G Izatt, et al. Mit hyperloop final report. *Massachusetts Institute of Technology, Cambridge, Massachusetts*, 2017.

[27] Zhaoyu Guo, Jie Li, and Danfeng Zhou. Study of a null-flux coil electrodynamic suspension structure for evacuated tube transportation. *Symmetry*, 11(10):1239, 2019.

[28] Renato Galluzzi, Salvatore Circosta, Nicola Amati, Andrea Tonoli, Angelo Bonfitto, Torbjörn A Lembke, and Milan Kertész. A multi-domain approach to the stabilization of electrodynamic levitation systems. *Journal of Vibration and Acoustics*, 142(6):061004, 2020.

[29] Salvatore Circosta, Renato Galluzzi, Nicola Amati, Andrea Tonoli, Angelo Bonfitto, Torbjörn A Lembke, and Milan Kertész. Passive multi-degree-of-freedom stabilization of ultra-high-speed maglev vehicles. *Journal of Vibration and Acoustics*, 143(6), 2021.

[30] Federica Fanigliulo. Design and control of an experimental test system for a linear electrodynamic levitation device. Master's thesis, Politecnico di Torino, 2021.

[31] Synchronous servomotors akm, 2004. Edition 03. URL: `https://www.kollmorgen.com/it-it/products/motors/servo/akm-series/akm-series-ac-synchronous-motors/servomotori-sincroni-akm/`.

[32] Akd^{TM} quick start, Edition: December 2015, Revision F. URL: https://www.kollmorgen.com/sites/default/files/public_downloads/AKD%20Quick%20Start%20EN%20%28REV%20E%29.pdf.

[33] Amplifier system mgcplus with display and control panel ab22a/ab32. URL: https://www.hbm.com/it/2261/mgcplus-data-acquisition-system-daq/?product_type_no=MGCplus.

[34] Geeplus electromechanical actuators catalogue 2019, vm108 - 2p30 datasheet. URL: https://www.geeplus.com/wp-content/uploads/2019/08/Voice_Coil_motor_VM108-2P30.pdf.